than the normal aorta, and the pressure-imposed test was useful for specimens whose weakest direction was unknown such as in the case of a diseased aorta.

ELECTRONIC SUPPLEMENTARY MATERIAL

The online version of this article (doi:10.1007/s13239-011-0067-1) contains supplementary material, which is available to authorized users.

ACKNOWLEDGMENTS

The authors thank patients who allowed us to use their aneurysm specimens. The present study was supported in part by Grants-in-Aid for Young Scientists (B) from the Ministry of Education, Culture, Sports, Science and Technology (MEXT) of Japan (No. 22700467) and the Science and Technology Promotion Adjustment Cost Program from the Japan Science and Technology Agency.

CONFLICT OF INTEREST

The authors have no financial and personal relationships with the other people or organizations that could inappropriately influence our work.

REFERENCES

[1]Cambria, R. A., P. Gloviczki, A. W. Stanson, K. J. Cherry, Jr., T. C. Bower, J. W. Hallett, Jr., *et al.* Outcome and expansion rate of 57 thoracoabdominal aortic aneurysms managed nonoperatively. *Am. J. Surg.* 170(2):213–217, 1995.

[2]Canham, P. B., H. M. Finlay, J. G. Dixon, and S. E. Ferguson. Layered collagen fabric of cerebral aneurysms quantitatively assessed by the universal stage and polarized light microscopy. *Anat. Rec.* 231(4):579–592, 1991.

[3]Coady, M. A., J. A. Rizzo, G. L. Hammond, D. Mandapati, U. Darr, G. S. Kopf, *et al.* What is the appropriate size criterion for resection of thoracic aortic aneurysms? *J. Thorac. Cardiovasc. Surg.* 113(3):476–491, 1997.

[4]Darling, R. C., C. R. Messina, D. C. Brewster, and L. W. Ottinger LW. Autopsy study of unoperated abdominal aortic aneurysms. The case for early resection. *Circulation* 56(3):II161–ii164, 1977.

[5]Fillinger, M. F., M. L. Raghavan, S. P. Marra, J. L. Cronenwett, and F. E. Kennedy. In vivo analysis of mechanical wall stress and abdominal aortic aneurysm rupture risk. *J. Vasc. Surg.* 36(3):589–597, 2002.

[6]Fukui, T., T. Matsumoto, T. Tanaka, T. Ohashi, K. Kumagai, H. Akimoto, *et al.* In vivo mechanical properties of thoracic aortic aneurysmal wall estimated from in vitro biaxial tensile test. *Biomed. Mater. Eng.* 15(4):295–305, 2005.

[7]Groenink, M., S. E. Langerak, E. Vanbavel, E. E. van der Wall, B. J. Mulder, A. C. van der Wal, *et al.* The influence of aging and aortic stiffness on permanent dilation and breaking stress of the thoracic descending aorta. *Cardiovasc. Res.* 43(2):471–480, 1999.

[8]Johansson, G., U. Markstrom, and J. Swedenborg. Ruptured thoracic aortic aneurysms: a study of incidence and mortality rates. *J. Vasc. Surg.* 21(6):985–988, 1995.

[9]Kato, Y., T. Matsumoto, K. Kumagai, H. Akimoto, K. Tabayashi, and M. Sato. Development of a simple method to construct finite element models of aortas from MRI images and its application to thoracic aortic aneurysm. *JSME Int. J. Ser. C* 43(4):787–794, 2000.

[10]Li, W. C., M. H. Yu, H. M. Zhang, H. Q. Wang, G. M. Xi, B. C. Yao, *et al.* Biomechanical properties of ascending aorta and pulmonary trunk in pigs and humans. *Xenotransplantation* 15(6):384–389, 2008.

[11]Matsumoto, T., T. Fukui, T. Tanaka, N. Ikuta, T. Ohashi, K. Kumagai, *et al.* Biaxial tensile properties of thoracic aortic aneurysm tissues. *J. Biomech. Sci. Eng.* 4(4):518–529, 2009.

[12]Ohashi, T., T. Matsumoto, H. Abe, T. Aoki, and M. Sato. Intramural distribution of local elastic moduli in bovine thoracic aorta measured by pipette aspiration method. *J. Cell Eng.* 2(1):12–18, 1997.

[13]Ohashi, T., S. Sugita, T. Matsumoto, K. Kumagai, H. Akimoto, K. Tabayashi, *et al.* Rupture properties of blood vessel walls measured by pressure-imposed test. *JSME Int. J. Ser. C* 46(4):1290–1296, 2003.

[14]Okamoto, R. J., J. E. Wagenseil, W. R. DeLong, S. J. Peterson, N. T. Kouchoukos, and T. M. Sundt, 3rd. Mechanical properties of dilated human ascending aorta. *Ann. Biomed. Eng.* 30(5):624–635, 2002.

[15]Raghavan, M. L., D. A. Vorp, M. P. Federle, M. S. Makaroun, and M. W. Webster. Wall stress distribution on three-dimensionally reconstructed models of human abdominal aortic aneurysm. *J. Vasc. Surg.* 31(4):760–769, 2000.

[16]Raghavan, M. L., M. W. Webster, and D. A. Vorp. Ex vivo biomechanical behavior of abdominal aortic aneurysm: assessment using a new mathematical model. *Ann. Biomed. Eng.* 24(5):573–582, 1996.

[17]Stemper, B. D., N. Yoganandan, M. R. Stineman, T. A. Gennarelli, J. L. Baisden, and F. A. Pintar. Mechanics of fresh, refrigerated, and frozen arterial tissue. *J. Surg. Res.* 139(2):236–242, 2007.

[18]Sterpetti, A. V., A. Cavallaro, N. Cavallari, P. Allegrucci, A. Tamburelli, F. Agosta, *et al.* Factors influencing the rupture of abdominal aortic aneurysms. *Surg. Gynecol. Obstet.* 173(3):175–178, 1991.

[19]Svensjo, S., H. Bengtsson, and D. Bergqvist. Thoracic and thoracoabdominal aortic aneurysm and dissection: an investigation based on autopsy. *Br. J. Surg.* 83(1):68–71, 1996.

[20]The Population Survey Report 2007–2008 [database on the Internet]. Ministry of Health, Labor and Welfare, Japan. 2008. Accessed March 1, 2010, from http://www.mhlw.go.jp. .

[21]The Population Survey Report 2008–2009 [database on the Internet]. Ministry of Health, Labor and Welfare, Japan. 2009. Accessed March 1, 2010, from http://www.mhlw.go.jp.

[22]Wilson, K. A., A. J. Lee, P. R. Hoskins, F. G. Fowkes, C. V. Ruckley, and A. W. Bradbury. The relationship between aortic wall distensibility and rupture of infrarenal abdominal aortic aneurysm. *J. Vasc. Surg.* 37(1):112–117, 2003.

Ultrasound Obstet Gynecol 2012; 40: 476–478
Published online in Wiley Online Library (wileyonlinelibrary.com). DOI: 10.1002/uog.11114

High-intensity focused ultrasound treatment for twin reversed arterial perfusion sequence

K. ICHIZUKA*, J. HASEGAWA*, M. NAKAMURA*, R. MATSUOKA*, A. SEKIZAWA*, T. OKAI* and S. UMEMURA†

**Department of Obstetrics and Gynecology, School of Medicine, Showa University, Tokyo, Japan; †Graduate School of Biomedical Engineering, Tohoku University, Sendai, Japan*

KEYWORDS: fetal therapy; HIFU; high-intensity focused ultrasound; non-invasive; TRAP sequence

ABSTRACT

Twin reversed arterial perfusion (TRAP) sequence is a serious complication of monochorionic twin pregnancies, in which arterioarterial anastomoses allow blood flow from a 'pump' fetus to an acardiac fetus via reversed flow in the latter's umbilical artery. Several trial treatments for TRAP sequence have been reported, but all of these have been invasive. We present a case of TRAP sequence in which high-intensity focused ultrasound (HIFU) was applied to the umbilical artery of the anomalous twin at 26 weeks as a non-invasive fetal therapy. The HIFU intensity was set at approximately 2300 W/cm^2 with exposure periods of 10 s. Color Doppler ultrasound showed a decrease in blood supply to the anomalous twin, although complete occlusion of the targeted vessel was not achieved. Delivery was by Cesarean section at 29 weeks' gestation and the pump twin survived, without severe clinical complications at 6 months. Copyright © 2012 ISUOG. Published by John Wiley & Sons, Ltd.

CASE REPORT

A 23-year-old woman who had had no previous pregnancies conceived twins naturally. Ultrasound examination at 11 weeks' gestation detected heart beats in both fetuses; however, pleural effusion, ascites and severe structural anomalies were evident in one fetus. Amniotic fluid sampling from the sac of the normal twin was performed at 16 weeks' gestation, revealing a normal 46,XX karyotype. The edema of the abnormal twin gradually worsened and the patient was admitted to our hospital at 22 weeks.

Ultrasound examination following admission showed that the anomalous fetus had an underdeveloped head and upper extremities, severe subcutaneous edema, pleural effusion and ascites. There was a severely underdeveloped heart showing a trace of cardiac rhythm. However, blood flow pulsation in the systemic circulation of the anomalous fetus coincided with the heart beat of the normal fetus. An arterioarterial anastomosis was detected on the placental surface, which enabled blood flow from the normal fetus to the anomalous fetus. On Doppler ultrasound we observed reversed flow in the umbilical artery of the anomalous fetus. We concluded that the heart of the anomalous fetus was not functioning and that the blood supply to this fetus was supplied by the heart of the normal fetus, leading us to diagnose twin reversed arterial perfusion (TRAP) sequence.

Neither polyhydramnios nor signs of heart failure were identified in the normal fetus, but because the anomalous fetus displayed pronounced subcutaneous edema and fluid pooling, the decision was made at 26 weeks' gestation to apply ultrasound-guided high-intensity focused ultrasound (HIFU) to occlude the anastomosis and hence interrupt the blood flow to the anomalous fetus, thus reducing the cardiac load of the normal twin. The Ethics Committee for Clinical Studies approved the procedure and informed consent was obtained from the patient.

The target for HIFU exposure was the blood flow at the point where the umbilical cord entered the body of the anomalous fetus (Figures 1 and 2). The HIFU transducer used in this case had a focal length of 7 cm, and the methodology and settings for the procedure were derived from the findings of our previous experimental studies using animal models[1–6]. The HIFU intensity was set at approximately 2300 W/cm^2 with exposure periods of 10 s. Olive oil was used as the coupling agent; because olive oil can penetrate deeply and uniformly to the depths of wrinkles and pores in the skin and exclude air more effectively than normal ultrasound gel, it is possible to obtain improved ultrasound impedance coupling between the skin and the surface of the transducer. The safety of using olive oil as a coupling agent had been confirmed previously in animal experiments[4]. HIFU was administered several times and decreased umbilical blood flow to the anomalous fetus was confirmed by color Doppler imaging; however, complete occlusion was not achieved. Despite the failure to achieve complete occlusion, a hyperechoic area was observed just proximal to the targeted blood vessel, indicating degeneration of the tissue by exposure to HIFU (Figure 3). Collateral damage was not seen in either the pump fetus or the mother.

Polyhydramnios was diagnosed at 29 weeks' gestation in the normal twin, making premature birth an imminent threat, and a Cesarean section was performed. The pump twin weighed 845 g and was admitted to the neonatal intensive care unit with Apgar scores of 1 and 2 at 1 and 5 min, respectively. Severe subcutaneous skin edema contributed to the large size of the anomalous fetus, which weighed 2800 g (Figure 4). Following 6 months in intensive care the surviving infant will shortly (at the time of writing) be discharged without any severe clinical complications.

DISCUSSION

Preliminary research has been conducted in animal models in which HIFU was used to treat fetuses *in utero*[1–6]. These studies, which investigated the optimum intensity, ultrasound frequency and exposure time of HIFU, and evaluated its safety and effectiveness in arterial occlusion, led us to the conclusion that we can apply HIFU as a non-invasive treatment for human fetuses. TRAP sequence was selected as the most suitable fetal disorder for *in-utero* treatment with HIFU.

In this case, following HIFU treatment we observed a hyperechoic area just proximal to the targeted vessels

Correspondence to: Dr K. Ichizuka, Showa University, School of Medicine, Department of Obstetrics and Gynecology, 142-8666 Hatanodai Shinagawaku, Tokyo, Japan (e-mail: ichizuka@med.showa-u.ac.jp)

Accepted: 16 January 2012

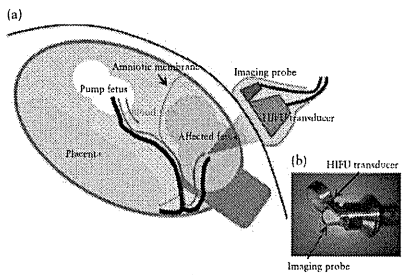

Figure 1 (a) Schematic diagram showing position of the fetuses in a case of twin reversed arterial perfusion sequence at time of high-intensity focused ultrasound (HIFU) procedure. The imaging probe is fixed to the HIFU transducer (b) and placed in a plastic bag, which is filled with degassed water.

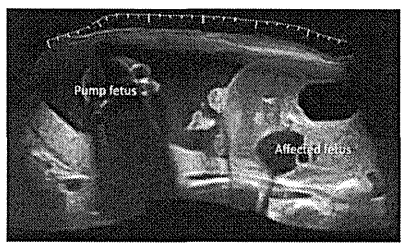

Figure 2 Extended-field-of-view ultrasound image of the two fetuses in a case of twin reversed arterial perfusion sequence prior to the high-intensity focused ultrasound procedure.

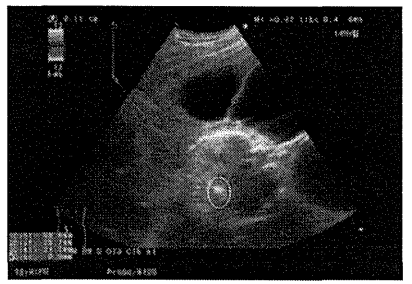

Figure 3 Ultrasound image showing a hyperechoic area (within white dotted line) that appeared after high-intensity focused ultrasound had been applied to the umbilical artery of the anomalous fetus in a case of twin reversed arterial perfusion sequence.

Figure 4 Photograph of the anomalous fetus showing underdeveloped head and upper extremities.

but did not achieve complete occlusion of blood flow to the anomalous fetus. In previous animal experiments, subsequent histological tests confirmed that denaturation due to heat had occurred at the site of HIFU exposure; this was visible as a hyperechoic area on ultrasound imaging[2,3]. We therefore believe that tissue denaturation was induced in the hyperechoic area observed in the present case.

One possible explanation for the incomplete occlusion of blood flow in this case is that the distance between the target and the maternal abdomen was larger than the focal distance of the HIFU transducer that we specifically made for this procedure. This disparity arose as a result of the rapid increase in edema in the anomalous fetus; the distance between the umbilicus of the anomalous fetus and uterine wall significantly increased within a matter of days. If this factor is taken into account, it should be possible to completely occlude the inflow vessels from the pump twin to the acardiac fetus in cases of TRAP sequence using HIFU.

TRAP sequence was formerly treated by selective delivery of the acardiac fetus[7]. However, as this is a highly invasive procedure, subsequent less invasive therapies with endoscopic techniques for TRAP sequence have been developed[8–13]. However, methods such as ultrasound-guided radiofrequency ablation still involve the insertion of devices into the uterus and direct contact with the fetus. This carries the risk of membrane rupture, premature birth and hemorrhage.

Although the procedure was not completely successful in this case, the possibility of inducing localized denaturation of human fetal tissue non-invasively using HIFU has been demonstrated for the first time, marking a step towards the more widespread use of HIFU in fetal treatment.

REFERENCES

1. Fujiwara R, Sasaki K, Ishikawa T, Suzuki M, Umemura S, Kushima M, Okai T. Arterial blood flow occlusion by high intensity focused ultrasound and histologic evaluation of its effect on arteries and surrounding tissues. *J Med Ultrasonics* 2002; **29**: 85–90.
2. Ishikawa T, Okai T, Sasaki K, Umemura S, Fujiwara R, Kushima M, Ichihara M, Ichizuka K. Functional and histological changes in rat femoral arteries by HIFU exposure. *Ultrasound Med Biol* 2003; **29**: 1471–1477.
3. Ichizuka K, Ando S, Ichihara M, Ishikawa T, Uchiyama N, Sasaki K, Umemura S, Matsuoka R, Sekizawa A, Okai T, Akabane T, Kushima M. Application of high-intensity focused ultrasound for umbilical artery occlusion in a rabbit model. *Ultrasound Obstet Gynecol* 2007; **30**: 47–51.
4. Ichizuka K, Aoki H, Ichihara M, Matsuoka R, Hasegawa J, Okai T. Application of high-intensity focused ultrasound for fetal therapy – experimental study using animal model for obstructive uropathy. *Ultrasound Obstet Gynecol* 2008; **32**: 387.
5. Ishikawa T, Okai T, Sasaki K, Umemura S, Miyazaki N, Kushima M, Aoki H, Ichihara M, Ichizuka K. Sequential changes in rat femoral artery blood flow and tissue degeneration after exposure to high-intensity focused ultrasound. *J Med Ultrasonics* 2008; **35**: 177–182.
6. Aoki H, Ichizuka K, Ichihara M, Okai T, Kushima M. Experiment of high-intensity focused ultrasound (HIFU) exposure for surface blood vessel of placenta – potential for therapy of TTTS. *Ultrasound Obstet Gynecol* 2009; **34**: 134.
7. Robie GF, Payne GG Jr, Morgan MA. Selective delivery of an acardiac, acephalic twin. *N Engl J Med* 1989; **320**: 512–513.
8. McCurdy CM Jr, Childers JM, Seeds JW. Ligation of the umbilical cord of an acardiac–acephalus twin with an endoscopic intrauterine technique. *Obstet Gynecol* 1993; **82**: 708–711.
9. Hecher K, Hackeloer BJ, Ville Y. Umbilical cord coagulation by operative microendoscopy at 16 weeks' gestation in an acardiac twin. *Ultrasound Obstet Gynecol* 1997; **10**: 130–132.
10. Quintero RA, Chmait RH, Murakoshi T, Pankrac Z, Swiatkowska M, Bornick PW, Allen MH. Surgical management of twin reversed arterial perfusion sequence. *Am J Obstet Gynecol* 2006; **194**: 982–991.
11. Hecher K, Lewi L, Gratacos E, Huber A, Ville Y, Deprest J. Twin reversed arterial perfusion: fetoscopic laser coagulation of placental anastomoses or the umbilical cord. *Ultrasound Obstet Gynecol* 2006; **28**: 688–691.
12. Tsao K, Feldstein VA, Albanese CT, Sandberg PL, Lee H, Harrison MR, Farmer DL. Selective reduction of acardiac twin by radiofrequency ablation. *Am J Obstet Gynecol* 2002; **187**: 635–640.
13. Hirose M, Murata A, Kita N, Aotani H, Takebayashi K, Noda Y. Successful intrauterine treatment with radiofrequency ablation in a case of acardiac twin pregnancy complicated with a hydropic pump twin. *Ultrasound Obstet Gynecol* 2004; **23**: 509–512.

Hemodynamic Analysis of Growing Intracranial Aneurysms Arising from a Posterior Inferior Cerebellar Artery

Shin-Ichiro Sugiyama[1], Hui Meng[3,4], Kenichi Funamoto[4], Takashi Inoue[2], Miki Fujimura[2], Toshio Nakayama[4], Shunsuke Omodaka[6], Hiroaki Shimizu[2], Akira Takahashi[6], Teiji Tominaga[5]

Key words
- Hemodynamics
- Intracranial aneurysm
- Wall shear stress

Abbreviations and Acronyms
3D: Three-dimensional
CFD: Computational fluid dynamics
MR: Magnetic resonance
OSI: Oscillatory shear index
PICA: Posterior inferior cerebellar artery
VA: Vertebral artery
WSS: Wall shear stress

From the Departments of [1]Neuroanesthesia and [2]Neurosurgery, Kohnan Hospital, Sendai, Japan; [3]Toshiba Stroke Research Center, University at Buffalo, The State University of New York, Buffalo, New York, USA; [4]Institute of Fluid Science, Tohoku University, Sendai, Japan; and Departments of [5]Neurosurgery and [6]Neuroendovascular Therapy, Tohoku University Graduate School of Medicine, Sendai, Japan

To whom correspondence should be addressed: Shin-ichiro Sugiyama, M.D., Ph.D. [E-mail: sushi@kohnan-sendai.or.jp]

Citation: World Neurosurg. (2012) 78, 5:462-468.
DOI: 10.1016/j.wneu.2011.09.023
*Journal homepage: **www.WORLDNEUROSURGERY.org***
*Available online: **www.sciencedirect.com***
1878-8750/$ - see front matter

OBJECTIVE: The role of hemodynamics in the growth of intracranial aneurysms is not completely clear. We present a hemodynamic study with two adjacent unruptured aneurysms arising from one parent artery but growing in different ways. This study aimed to investigate whether there were differences in hemodynamic characteristics between the two growing aneurysms.

METHODS: A 62-year-old female patient presented with six unruptured intracranial aneurysms. Catheter angiography at 6-month intervals revealed that two aneurysms located adjacently at the right posterior inferior cerebellar artery were growing over a 1-year period. Three-dimensional aneurysm geometries were acquired via rotational angiography. Computational fluid dynamic simulations were conducted on the 3D aneurysm geometries under patient-specific pulsatile flow conditions that were measured by magnetic resonance velocimetry.

RESULTS: The proximal multilobular aneurysm demonstrated high flow and physiological levels of wall shear stress (WSS) in the region of growth, whereas the distal rounded aneurysm had low flow and low WSS in the growing sac.

CONCLUSION: Growing aneurysms can have heterogeneous hemodynamic and morphologic characteristics and different growing patterns. Growing regions of an aneurysm could be exposed to either high WSS at the inflow zone or low WSS and high oscillatory shear in the aneurysm sac.

INTRODUCTION

Hemodynamics is thought to influence the initiation, growth, and rupture of intracranial aneurysms (16). Although there seems to be general consensus that high wall shear stress (WSS) results in the initiation of intracranial aneurysms (13-16), the hemodynamic conditions that drive the growth of aneurysms after initiation are still not completely clear. High WSS has been postulated to account for aneurysm progression from the distal neck where flow impinges (6, 8), whereas low WSS has been associated with aneurysm growth in the dome (1, 18, 19).

We present a hemodynamic study of two adjacent aneurysms originating from one parent artery but growing in different ways. Longitudinal data sets of 3D rotational angiography were used to reconstruct accurate geometries of the aneurysms and adjacent arteries. The purpose of this study was to determine whether there were differences in the hemodynamic characteristics of the two growing aneurysms.

MATERIALS AND METHODS

Case Presentation

A 62-year-old hypertensive female patient presented with vertigo. Computed tomographic imaging showed no evidence of hemorrhage but the presence of multiple intracranial aneurysms. Magnetic resonance (MR) angiography performed in April 2009 revealed six intracranial aneurysms: two in the right middle cerebral artery, two adjacent ones in the right posterior inferior cerebellar artery (PICA), one in the left middle cerebral artery, and one at the tip of the basilar artery (**Figure 1**). The two right middle cerebral artery aneurysms were clipped in May 2009, and the basilar tip aneurysm was treated via coil embolization in August 2009. The presurgical angiographic data were inaccessible digitally because of the unfortunate failure of a data storage device. The angiograph acquired during the coiling was therefore defined as the baseline for computational fluid dynamic (CFD) analysis. Thereafter, the patient's progress was followed up by angiography at 6-month intervals (first follow-up in February 2010; second follow-up in August 2010).

Between the initial angiograph and that obtained during embolization of the basilar tip aneurysm, the three untreated aneurysms showed no detectable change in shape or size. However, the two follow-up angiographs revealed that the two aneurysms in the right PICA had grown over time (**Figure 2**). The proximal multilobular aneurysm at the PICA–vertebral artery (VA) junction (Aneurysm 1) showed partial enlargement of the aneurysm wall, whereas the distal, more spherical aneurysm (Aneurysm 2) showed enlargement of the whole aneurysm body.

One month after the last angiography, the two growing PICA aneurysms were clipped individually via open occipital craniotomy. Aneurysm 1 had yellow blebs with atherosclerosis, whereas Aneurysm 2 was reddish and thin walled (**Figure 3**).

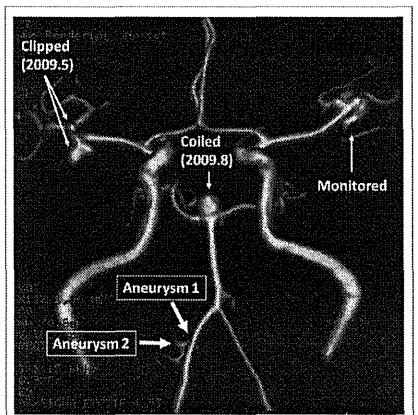

Figure 1. Magnetic resonance angiography at the initial presentation in April 2009 showing six aneurysms in this patient: two in the right middle cerebral artery, which were clipped in May 2009; one at the tip of the basilar artery, which was coiled in August 2009; and one in the left middle cerebral artery and two in the right posterior inferior cerebellar artery (PICA), referred to as Aneurysm 1 and Aneurysm 2.

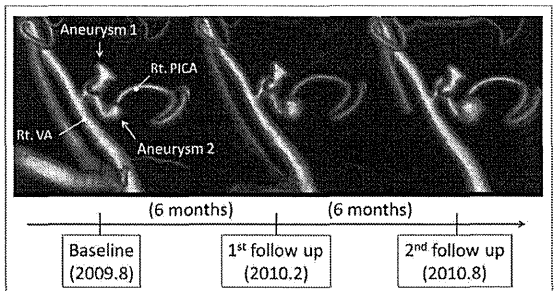

Figure 2. Three-dimensional rotational digital angiography of the two PICA aneurysms at three time points: baseline (August 2009), first follow-up (February 2010), and second follow-up (August 2010), showing that they grew over time. Both aneurysms were subsequently clipped in September 2010. PICA, posterior inferior cerebellar artery; Rt., right; VA, vertebral artery.

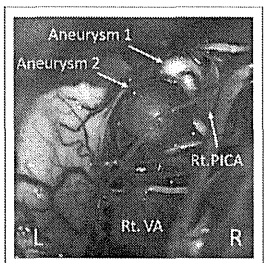

Figure 3. Intraoperative photograph showing two growing aneurysms originating in the right PICA. The proximal aneurysm (Aneurysm 1) had a yellowish wall with atherosclerosis, whereas the distal one (Aneurysm 2) had a reddish and rather thin wall. PICA, posterior inferior cerebellar artery; Rt., right; VA, vertebral artery.

Vessel and Aneurysm Modeling

Digital angiography was performed by standard transfemoral catheterization of the right VA, and digital imaging was performed using a biplanar unit (Innova 3131; General Electric Healthcare Japan, Tokyo, Japan). These images were obtained during a 6-second injection of a contrast agent and a 200-degree rotation with imaging at 30 frames per second for a total of 8 seconds. The corresponding 150 projection images were reconstructed into a 3D data set consisting of 512 × 512 × 512 isotropic voxels covering a field of view of 20 mm in all three directions. The images were reconstructed using a dedicated workstation.

The data set was exported to a personal computer to form 3D isosurfaces of the aneurysm using imaging software (Avizo 6.2; Visualization Science Group, Merignac, France). To provide consistent geometries from the data at three different time points, we identified on the baseline data set a reference vessel segment—the right VA—that remained unchanged over time. The mean value of the right VA was calculated, and one-half of the mean value was selected as the first threshold for defining intraluminal vessel volume. The segmented luminal surface was then displayed on native axial, coronal, and sagittal slices of 3D angiographic images until the displayed luminal surface visually matched the luminal boundary of all regions of interest. To provide a consistent threshold from baseline to follow-ups,

the three geometries were semiautomatically coregistered, and thresholds were adjusted to maintain the same reference diameter in subsequent segmentations.

The entire model of the aneurysm complex, including both PICA aneurysms, was created using commercial software (Magics RP 13.1; Materialise, Leuven, Belgium). Care was taken to ensure proper length of the parent artery (VA). The volumetric grid, composed of tetrahedral elements, was generated using meshing software (Gambit 2.4; ANSYS Inc., Lebanon, New Hampshire, USA) with a resolution of 0.1 mm, resulting in approximately 1.5 million element meshes.

Quantitative MR Velocimetry

Quantitative MR velocimetry was performed on this patient using a 3-Tesla MR image scanner (Signa HDxt 3.0T: General Electric Healthcare Japan) just before the last angiography. The protocol entails performing a standard axial 2D time-of-flight MR angiography of the cranial vasculature to select a slice orientation for the arterial blood flow measurements. The optimal perpendicular scan plane was determined using the acquired time of flight images. The coordinates obtained specify the position of an oblique fast 2D phase-contrast sequence, which was then performed based on these coordinates using a peripheral gated 2D phase-contrast sequence with the following imaging parameters: repetition time, 25; echo time, 5.4; number of excitations, 1; field of view, 160 × 160 mm; matrix, 512 × 512; voxel size, 0.3 × 0.3 mm; velocity encoding, 100 and 50 cm/s for the VA and PICA, respectively; imaging time, approximately 5 minutes; transaxial direction; peripheral gated with electrocardiography, 30 phases. The phase-contrast images were transferred to the workstation for flow quantification using dedicated software (CV flow; General Electric Healthcare Japan). A region of interest was semiautomatically placed on the phase-contrast images over one cardiac cycle. The velocities at all of the pixels inside the vessel border were integrated to calculate the flow in milliliters per minute. The quantitative waveform over one cardiac cycle was then drawn using these flow rates.

The flow rates were 83.3 and 12.2 mL/min in the right VA and right PICA, respectively. The waveform for the right VA was used as the inlet condition in numerical simulations, and the calculated fractional flow rates were specified for two outlet boundaries: 0.15 for the right PICA and 0.85 for the right VA.

CFD Simulations

Following the conventions for CFD in large vessels (3), blood was treated as an incompressible Newtonian fluid; vessel walls were assumed rigid, and no-slip boundary conditions were applied at the walls. A finite-volume package, Fluent (ANSYS Inc), was used to solve the governing equations: 3D unsteady Navier-Stokes equations and the equation of continuity. Patient-specific pulsatile flow conditions, derived from the MR velocimetry at the second follow-up, were prescribed at the inlet boundary (the right VA) of the three models. It was assumed that the waveform does not change appreciably over time. The diffusion fluxes in the direction normal to the inlet plane were assumed to be zero, and normal gradients were neglected. For the two outlet boundaries, we specified the fractional flow rate through each outlet calculated from the results of the MR velocimetry. A total of three cardiac cycles were computed using 100 time-steps per cycle; the results for the third cycle are presented.

Data Analysis

To visualize flow patterns, 3D streamlines of intra-aneurysm flow at peak systole and end diastole exiting the PICA were plotted in the model at each time point (baseline, first follow-up, and second follow-up) using commercial software (ANSYS CFD; ANSYS Inc).

WSS refers to the tangential frictional stress caused by the action of blood flow on the vessel wall. For pulsatile flow, the time-averaged WSS was calculated by integrating WSS magnitude over a cardiac cycle for each tetrahedral element (9):

$$WSS = \frac{1}{T}\int_0^T \left|\vec{\tau}_w\right| dt,$$

where $\vec{\tau}$ is the instantaneous WSS vector and T is the duration of the cycle. Because low WSS has been associated with aneurysm growth and rupture (18, 19, 22), we calculated WSS for the entire model at each time point.

To describe the temporal disturbance of intra-aneurysm flow, oscillatory shear index (OSI), a dimensionless measure of directional changes in WSS, was calculated using the formula reported by He and Ku (7):

$$OSI = \frac{1}{2}\left[1 - \frac{\left|\int_0^T \vec{\tau}_w dt\right|}{\int_0^T \left|\vec{\tau}_w\right| dt}\right].$$

Note that $0 \le OSI < 0.5$, with 0 being completely unidirectional shear and 0.5 being completely oscillatory. Because high OSI has been shown to be significant for ruptured aneurysms (22), we suspected that it might also be related to aneurysm growth. Therefore, we calculated the OSI for the entire model at each time point.

RESULTS

Figure 4A shows reconstructed 3D models of the PICA aneurysm complex from the three angiographs: the baseline and two follow-ups. To clearly visualize the regions of aneurysm growth, we overlapped three models by aligning the VA to achieve accurate matching, because this parent artery experienced no change over the observation period (**Figure 4B**). Clearly, the proximal aneurysm (Aneurysm 1) grew slightly on the superior side, whereas the distal aneurysm (Aneurysm 2) showed enlargement of the whole aneurysm body. Aneurysm 1, which was complex shaped with four blebs, grew in the region of the small bleb at the top, whereas the round-shaped Aneurysm 2 showed drastic enlargement of the whole sac. The extended tip at the bottom of Aneurysm 2 observed at the first follow-up suggests that its growth started from the bottom.

Figure 5 shows snapshots of the flow field (3D streamlines) captured at peak systole (A) and diastole (B). Note that the growing region of Aneurysm 1 experienced high-velocity flow. The inlet velocity waveform measured by MR velocimetry is also given.

Figure 6 shows the distribution of WSS and OSI in two views. Although **Figure 6A** presents the lateral view consistent with other figures presented above, the growing region in Aneurysm 1 cannot be examined in detail. To observe the growing region of Aneurysm 1 *en face*, we changed the viewing angle and plotted the results in **Figure 6B**.

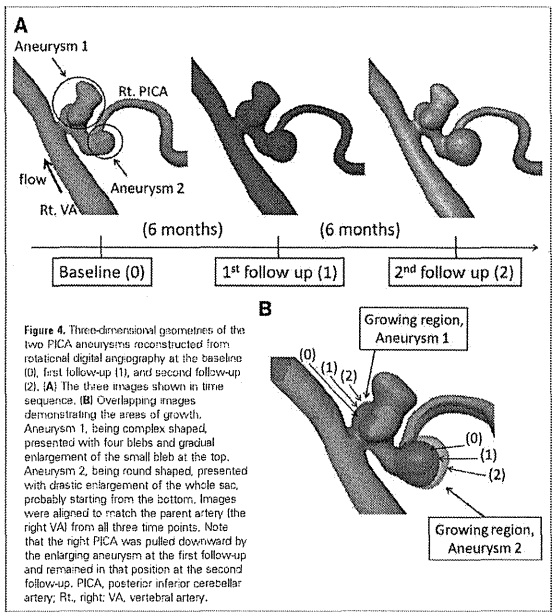

Figure 4. Three-dimensional geometries of the two PICA aneurysms reconstructed from rotational digital angiography at the baseline (0), first follow-up (1), and second follow-up (2). (**A**) The three images shown in time sequence. (**B**) Overlapping images demonstrating the areas of growth. Aneurysm 1, being complex shaped, presented with four blebs and gradual enlargement of the small bleb at the top. Aneurysm 2, being round shaped, presented with drastic enlargement of the whole sac, probably starting from the bottom. Images were aligned to match the parent artery (the right VA) from all three time points. Note that the right PICA was pulled downward by the enlarging aneurysm at the first follow-up and remained in that position at the second follow-up. PICA, posterior inferior cerebellar artery; Rt., right; VA, vertebral artery.

From **Figures 5** and **6**, it is evident that the growing area in Aneurysm 1 (a mild bleb on the top) was located near the inflow zone and therefore experienced high-velocity flow near the wall, as shown by the colored streamlines in **Figure 5**. This growing region was subjected to physiological levels of WSS (0.45–1.20 Pa) (10, 18), much higher than the WSS (~0.30 Pa) experienced by the more protruded blebs on Aneurysm 1. As this bleb enlarged, its WSS decreased. The OSI in the growing bleb was initially lower than that in the other blebs but increased with time.

Aneurysm 2, on the other hand, experienced low intra-aneurysm flow in its growing sac. It started with a rather low WSS (0.02–0.45 Pa) and a high OSI (~0.29) at the baseline; as the whole sac enlarged, the WSS sequentially decreased and the OSI sequentially increased. Time-resolved visualization (not shown) revealed that the flow field in Aneurysm 2 was unstable, with the flow divisions and vortex structures moving around during the cardiac cycle (12). The intra-aneurysm flow during the cardiac cycle became more and more unstable as the aneurysm sac enlarged, which is consistent with the increase in the OSI.

DISCUSSION

The purpose of this study was to determine whether there were differences in the hemodynamics of two adjacent aneurysms that presented different morphologic and vascular characteristics and were growing in different ways. One aneurysm (Aneurysm 1), which was multilobular in shape, already had three prominent protrusions (lobes) with an atherosclerotic wall. During the examination period, it was seen to grow on a fourth bleb. The other aneurysm (Aneurysm 2) was reddish, thin walled, and round. It grew rapidly by enlargement of the whole sac during the time interval before the next follow-up. Flow simulations revealed that the growing bleb of the multilobular aneurysm was located near the inflow zone and demonstrated high-velocity flow and physiological levels of WSS. In contrast, the large round aneurysm showed low intra-aneurysm flow, low WSS levels, and unstable flow patterns (higher OSI) in the dome. We speculate that the differences in the hemodynamic, morphological, and vascular characteristics of these two aneurysms indicate different mechanisms for their growth.

Regarding the partial growth of Aneurysm 1, high WSS has been postulated to account for aneurysm progression from the distal neck, where flow is impeded (6, 8). Meng et al. have shown that in animal models, high flow impact leading to high WSS and steep gradients of stress can cause destructive remodeling of the wall and aneurysm initiation (12, 14, 15). Cebral et al. showed that high flow impact might be an indicator of bleb formation and that most blebs progress to low WSS states after the blebs are formed (4). Shojima et al. speculated that such flow impact produces a steep shear gradient near the impact zone and accelerates the low shear-mediated process on the aneurysm wall (18). These underlying mechanisms might explain the growth of Aneurysm 1 and suggest that the growing region of Aneurysm 1 was in the process of developing a bleb like the other three blebs on this aneurysm. The intraoperative view of Aneurysm 1 at the end of examination period did not expose the growing region; therefore, we do not know if the wall of the growing region was yellowish with atherosclerotic plaque like the other part of this aneurysm or if it was reddish and thin walled like Aneurysm 2.

The growth of Aneurysm 2, in a low shear stress environment, may be consistent with observations by Boussel et al. (1). In their excellent longitudinal study, seven growing aneurysms were followed using 1.5-T MR angiography and patient-specific CFD. They found that aneurysm growth occurred in the wall exposed to abnormally low WSS (1). Our simulations (with higher resolution geometries derived from 3D rotational angiography) produced similar results, showing association of low WSS with aneurysm growth. In addition to low WSS, we suggest

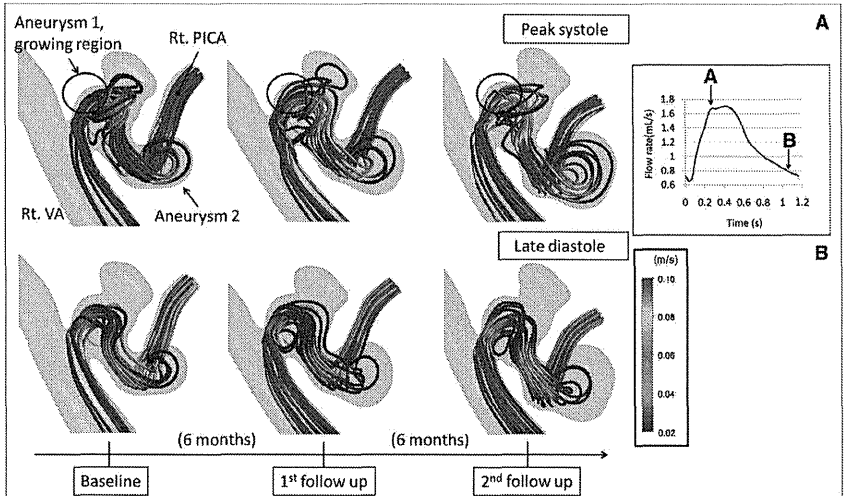

Figure 5. Snapshots of flow field (3D streamlines) captured at peak systole (**A**) and late diastole (**B**) as indicated on the inlet velocity waveform measured at the right vertebral artery by MR velocimetry during the second follow-up. The same waveform was used to run all three simulations. Note that the growing region of Aneurysm 1 experienced high flow near the entrance. PICA, posterior inferior cerebellar artery; Rt., right; 3D, three-dimensional; VA, vertebral artery.

that such aneurysm growth is associated with a high OSI, which indicates unstable, disturbed flow with significant directional change of WSS during the cardiac cycle. Xiang et al. found that WSS and the OSI are the significant hemodynamic factors that determine aneurysm rupture (22).

Our findings support those of Boussel et al. (1), suggesting a correlation between low aneurysmal flow hemodynamics and aneurysm growth. Our study did not indicate a causal relationship between the two, although such a relationship is entirely possible. Blood vessels can remodel in response to an abnormal hemodynamic environment (10). Aneurysm enlargement could be driven by biological processes mediated by unfavorable hemodynamic conditions such as low and oscillatory fluid shear stress, which have been shown to activate atherogenic and proinflammatory signaling pathways in endothelial cells (5, 11, 17). Activation of such inflammatory pathways might cause degradation of the aneurysm wall and growth of the aneurysm.

Our current study, based on patient-specific geometries, suggests that aneurysm growth is associated with a decrease in WSS and an increase in the OSI. Although it is not clear whether low WSS and a high OSI influence aneurysm growth, the reverse is almost certainly true: aneurysm geometry changes will result in changes of intra-aneurysm flow dynamics because geometry determines the flow. As demonstrated in numerical experiments by Tremmel et al. (21), aneurysm enlargement is followed by a decreased WSS on the aneurysm wall and often by an increased flow instability (the flow splits into multiple vortices that move around). Increased flow instability is accompanied by increased directional changes of fluid shear stress on the aneurysm wall, thus increasing the OSI.

The unanswered but highly intriguing question is whether certain hemodynamic factors, such as the high flow in the inflow zone of Aneurysm 1 and the disturbed flow in the dome of Aneurysm 2, are responsible for aneurysm growth. Further clinical studies are required to ascertain the significance of the relationship between hemodynamics and aneurysm history. In vivo studies are required to clarify the mechanobiological effects of hemodynamic factors on the aneurysm wall. Such an understanding could lead to exciting opportunities for predicting aneurysm growth by image-based CFD.

Our CFD simulations include typical simplifications made in model generation and boundary conditions (20). Several biological properties such as the viscoelasticity of the vessel wall and the non-Newtonian property of the blood are neglected for technical reasons. For the inlet condition, we used a pulsatile waveform obtained on this patient before the third angiography for all three simulations. It should be pointed out that this is an improvement over what has been typically done in CFD, where a non-patient-specific waveform is used as the inlet condition (2). We believe that despite these simplifications, our CFD analysis has captured the main hemodynamic features of growing aneurysms. The region of aneu-

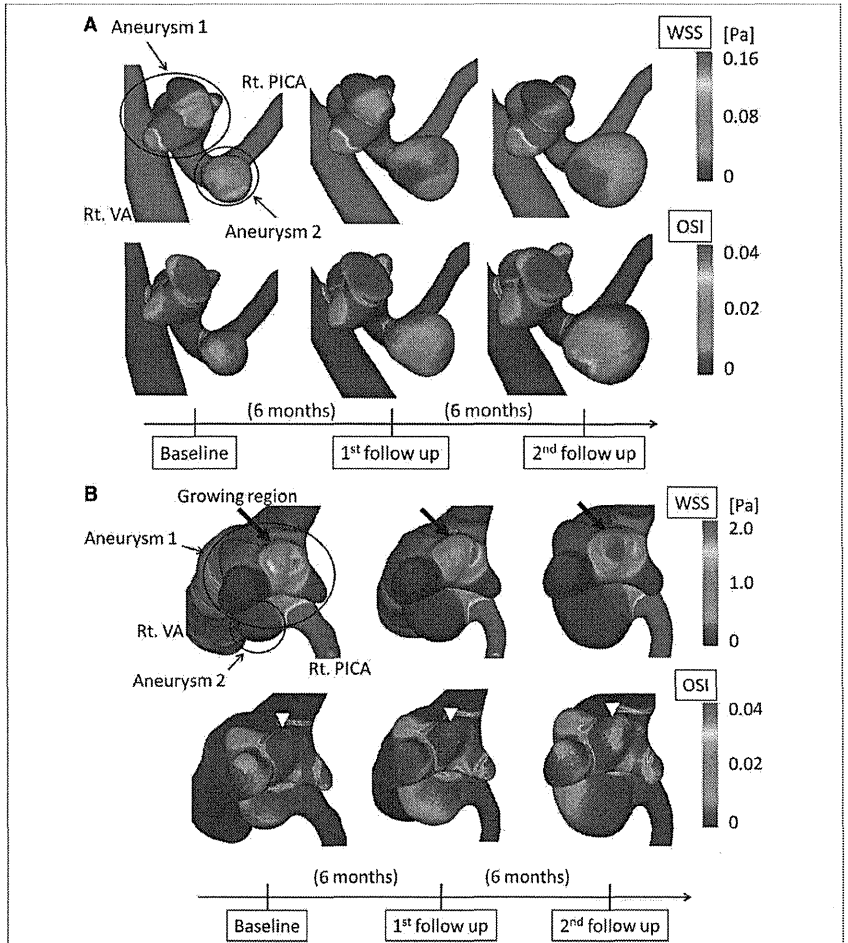

Figure 6. Distribution of time-averaged wall shear stress (WSS) and oscillatory shear index (OSI) in two views. (**A**) Lateral view consistent with **Figures 2–5**; (**B**) En face view of the growing area in Aneurysm 1 (blood in VA comes towards the reader). As evident from B, the growing region of Aneurysm 1 experienced higher WSS and lower OSI than the more protruded blebs; however, as this bleb enlarged, the WSS is seen to decrease (black arrow) and OSI to slightly increase (white arrowhead) with time. Aneurysm 2, on the other hand had rather low WSS (seen from both A and B) and high OSI (seen from A) to start with, and as the whole sack enlarged, the WSS continued to decrease and OSI continued to increase. Note that the scale of WSS in A is smaller than that in B. PICA, posterior inferior cerebellar artery; Rt., right; VA, vertebral artery.

rysm growth could experience either high WSS at the inflow zone or low WSS and a high OSI in the aneurysm sac.

CONCLUSIONS

We have shown two growing aneurysms with different hemodynamic characteristics and growing patterns: a proximal multilobular aneurysm was growing a bleb near the inflow zone with high local velocity and physiological levels of WSS, whereas a distal rounded aneurysm was growing the entire sac featuring low and unstable intra-aneurysmal flow, with low WSS and higher OSI. Thus, growing aneurysms may have heterogeneous hemodynamic, morphologic, and vascular characteristics associated with different mechanistic pathways.

REFERENCES

1. Boussel L, Rayz V, McCulloch C, Martin A, Acevedo-Bolton G, Lawton M, Higashida R, Smith WS, Young WL, Saloner D: Aneurysm growth occurs at region of low wall shear stress: patient-specific correlation of hemodynamics and growth in a longitudinal study. Stroke 39:2997-3002, 2008.

2. Cebral JR, Mut F, Weir J, Putman CM: Association of hemodynamic characteristics and cerebral aneurysm rupture. AJNR Am J Neuroradiol 32:264-270, 2011.

3. Cebral JR, Mut F, Weir J, Putman C: Quantitative characterization of the hemodynamic environment in ruptured and unruptured brain aneurysms. AJNR Am J Neuroradiol 32:145-151, 2011.

4. Cebral JR, Sheridan M, Putman CM: Hemodynamics and bleb formation in intracranial aneurysms. AJNR Am J Neuroradiol 31:304-310, 2010.

5. Chiu JJ, Chen CN, Lee PL, Yang CT, Chuang HS, Chien S, Usami S: Analysis of the effect of disturbed flow on monocytic adhesion to endothelial cells. J Biomech 36:1883-1895, 2003.

6. Hashimoto T, Meng H, Young WL: Intracranial aneurysms: links among inflammation, hemodynamics and vascular remodeling. Neurol Res 28:372-380, 2006.

7. He X, Ku DN: Pulsatile flow in the human left coronary artery bifurcation: average conditions. J Biomech Eng 118:74-82, 1996.

8. Hoi Y, Meng H, Woodward SH, Bendok BR, Hanel RA, Guterman LR, Hopkins LN: Effects of arterial geometry on aneurysm growth: three-dimensional computational fluid dynamics study. J Neurosurg 101:676-681, 2004.

9. Lee SW, Antiga L, Steinman DA: Correlations among indicators of disturbed flow at the normal carotid bifurcation. J Biomech Eng 131:061013, 2009.

10. Malek AM, Alper SL, Izumo S: Hemodynamic shear stress and its role in atherosclerosis. J Am Med Assoc 282:2035-2042, 1999.

11. Malek AM, Higashida RT, Halbach VV, Phatouros CC, Meyers PM, Dowd CF: Tandem intracranial stent deployment for treatment of an iatrogenic, flow-limiting, basilar artery dissection: technical case report. Neurosurgery 45:919-924, 1999.

12. Meng H, Metaxa E, Gao L, Liaw N, Natarajan SK, Swartz DD, Siddiqui AH, Kolega J, Mocco J: Progressive aneurysm development following hemodynamic insult. J Neurosurg 114:1095-1103, 2011.

13. Meng H, Swartz DD, Wang Z, Hoi Y, Kolega J, Metaxa EM, Szymanski MP, Yamamoto J, Sauvageau E, Levy EI: A model system for mapping vascular responses to complex hemodynamics at arterial bifurcations in vivo. Neurosurgery 59:1094-1100, 2006.

14. Meng H, Wang Z, Hoi Y, Gao L, Metaxa E, Swartz DD, Kolega J: Complex hemodynamics at the apex of an arterial bifurcation induces vascular remodeling resembling cerebral aneurysm initiation. Stroke 38:1924-1931, 2007.

15. Metaxa E, Tremmel M, Natarajan SK, Xiang J, Paluch RA, Mandelbaum M, Siddiqui AH, Kolega J, Mocco J, Meng H: Characterization of critical hemodynamics contributing to aneurysmal remodeling at the basilar terminus in a rabbit model. Stroke 41:1774-1782, 2010.

16. Nixon AM, Gunel M, Sumpio BE: The critical role of hemodynamics in the development of cerebral vascular disease. J Neurosurg 112:1240-1253, 2010.

17. Passerini AG, Polacek DC, Shi C, Francesco NM, Manduchi E, Grant GR, Pritchard WF, Powell S, Chang GY, Stoeckert CJ Jr, Davies PF: Coexisting proinflammatory and antioxidative endothelial transcription profiles in a disturbed flow region of the adult porcine aorta. Proc Natl Acad Sci U S A 101:2482-2487, 2004.

18. Shojima M, Nemoto S, Morita A, Oshima M, Watanabe E, Saito N: Role of shear stress in the blister formation of cerebral aneurysms. Neurosurgery 67:1268-1274, 2010.

19. Shojima M, Oshima M, Takagi K, Torii R, Hayakawa M, Katada K, Morita A, Kirino T: Magnitude and role of wall shear stress on cerebral aneurysm: computational fluid dynamic study of 20 middle cerebral artery aneurysms. Stroke 35:2500-2505, 2004.

20. Steinman DA, Taylor CA: Flow imaging and computing: large artery hemodynamics. Ann Biomed Eng 33:1704-1709, 2005.

21. Tremmel M, Dhar S, Levy EI, Mocco J, Meng H: Influence of intracranial aneurysm-to-parent vessel size ratio on hemodynamics and implication for rupture: results from a virtual experimental study. Neurosurgery 64:622-630, 2009.

22. Xiang J, Natarajan SK, Tremmel M, Ma D, Mocco J, Hopkins LN, Siddiqui AH, Levy EI, Meng H: Hemodynamic-morphologic discriminants for intracranial aneurysm rupture. Stroke 42:144-152, 2011.

Conflict of interest statement: The authors declare that the research was conducted in the absence of any commercial or financial relationships that could be construed as a potential conflict of interest. H. M. receives grants from the National Institutes of Health.

Received 04 July 2011; accepted 06 September 2011; published online 01 November 2011

Citation: World Neurosurg. (2012) 78, 5:462-468.
DOI: 10.1016/j.wneu.2011.09.023

*Journal homepage: **www.WORLDNEUROSURGERY.org***

*Available online: **www.sciencedirect.com***

1878-8750/$ - see front matter © 2012 Elsevier Inc.

A FORUM FOR SIX CONTINENTS

WORLD NEUROSURGERY

THE OFFICIAL JOURNAL OF THE WORLD FEDERATION OF NEUROSURGICAL SOCIETIES

電気学会論文誌 C（電子・情報・システム部門誌）
IEEJ Transactions on Electronics, Information and Systems
Vol.132 No.12 pp.1943–1948　DOI: 10.1541/ieejeiss.132.1943

論　文

植込み型除細動器への実装を考慮した致死性不整脈検出アルゴリズムの改良

正　員　阿部　　誠*　非会員　吉澤　　誠**　非会員　テルマ　ケイコ　スガイ***
非会員　本間　経康**　非会員　杉田　典大*　非会員　清水　一夫****
非会員　後藤　　萌****　非会員　稲垣　正司*5　非会員　杉町　　勝*5
非会員　砂川　賢二*6

Improving Detection Algorithm of Life-threatening Arrhythmias for Implementation of Implantable Cardioverter-Defibrillators

Makoto Abe*, Member, Makoto Yoshizawa**, Non-member, Telma Keiko Sugai***, Non-member, Noriyasu Homma**, Non-member, Norihiro Sugita*, Non-member, Kazuo Shimizu****, Non-member, Moe Goto****, Non-member, Masashi Inagaki*5, Non-member, Masaru Sugimachi*5, Non-member, Kenji Sunagawa*6, Non-member

(2012年2月29日受付，2012年6月28日再受付)

The implantable cardioverter-defibrillator (ICD) is an effective therapeutic device for rescuing patients with cardiac diseases from death caused by life-threatening arrhythmias. The authors previously proposed a detection algorithm of life-threatening arrhythmias with a multiple regression model. To enhance the classification accuracy, in the present study, we have introduced an autoregressive filter and a multiple detection process into the previous detection algorithm. The experimental results showed that the proposed method could attain a high accuracy such that all ventricular fibrillation rhythms could be exactly detected. In addition, detection errors of sinus rhythms or supraventricular tachyarrhythmias provoking the ICD malfunction were reduced.

キーワード：植込み型除細動器，致死性不整脈，重回帰モデル
Keywords: implantable cardioverter-defibrillator, life-threatening arrhythmia, multiple regression model

1. はじめに

日本における心血管系疾患に起因する心臓突然死による年間死者数は6万人以上といわれており，その対策は医学的かつ社会的な課題となっている[1]。心臓突然死において心臓が停止する直接の原因は，心室頻拍（VT: Ventricular Tachycardia）や心室細動（VF: Ventricular Fibrillation）といわれる心室性頻脈性不整脈であり，全体の80～90%を占める[2][3]。これらの致死性不整脈は，心疾患を抱えている患者のみならず，健康な子どもや成人のスポーツ選手であっても突如として発症することがある。そこで，近年では，自動体外式除細動器（AED: Automated External Defibrillator）が学校や公共施設に設置され，その普及によって発症後の救命率が上がっている。一方，このような致死性不整脈は再発率が高いと言われており，致死性不整脈発作を起こした患者の再発後の早期治療システムが必要である。そこで，1960年代にMirowskiらにより植込み型除細動器（ICD: Implantable Cardioverter Defibrillator）と呼ばれる装置が提唱され，実用化に至っている[4]。

現在は，洞性頻拍および上室性不整脈（SVT: supraventricular tachyarrhythmia）などの致死性でない不整脈に対する誤作動を防ぐため，心房内電位もモニタすることで致死性不整脈の鑑別をより確実に行う第5世代ICDが臨床使用されている[5]。しかし，既存のICDにおける不整脈検出アルゴリズムでは，主として心電図（ECG: electrocardiogram）の時間間隔情報に基づいてVFやVTの発生検出を行っているものがほとんどであるため，VFとVTを確実に区別することが困難である。また，一方でICDが致死的ではない不整脈を誤認して不適切な治療が行われることがあり[6]~[8]，致死性不整脈を的確に検出するICDの開発が急務とされている。

従来の方法に対し，われわれの研究グループでは，複数の心内心電図信号（IECG: Intracardiac electrocardiogram）から複数の指標を求め，それらを説明変数とし，不整脈の種類を目的変数とする重回帰モデルを用いる方法を提案し，高精度かつ早期の不整脈検出が可能であることを示してきた[9][10]。この提案方法によって，R-R間隔以外の情報も用いることで，不整脈をより柔軟に特徴づけることが可能となっている。しかし，それらの研究では，モデルへの入力として用いたデータに含まれる不整脈（SVT, VT, VF）の割合が，正常洞調律（SR: sinus rhythm）の割合に比べてかなり少なく，このことが誤検出の原因となっていた。そのため，VFの不検出率を0に近づけることが難しく，臨床応用上問題となる可能性があった。

そこで，本研究では，不整脈の割合がSRに比べて小さいデータ群において，誤検出の少ない重回帰モデルの作成方法を提案する。さらに，先行研究[10]の方法をさらに発展させることで，VFの不検出率を0に近づけるとともに，ICDの誤作動の原因となる誤検出をできるだけ減らすことを目的とする。

2. 方　法

〈2・1〉 実験データとその処理　本研究では，先行研究[9][10]と同様に，5頭の成犬を対象とした急性実験のデータを用いた。データは，左心室内（$IECG_{LV}$），右心室内（$IECG_{RV}$），および右心房内（$IECG_{RA}$）において取得した心内心電図であり，250 Hzにて再サンプリングを行ったものを用いた。なお，不整脈の自然発生を計測するのは困難であるため，電気刺激によってFig.1のようにSVT, VTおよびVFを模擬した。なお，データには1度だけ自然発生したVFも含まれている。

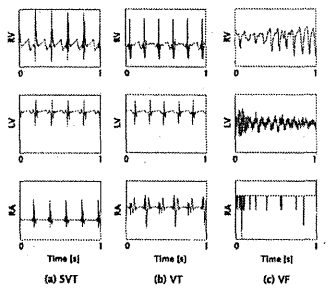

Fig. 1. Examples of IECG signals of (a) SVT, (b) VT, and (c) VF

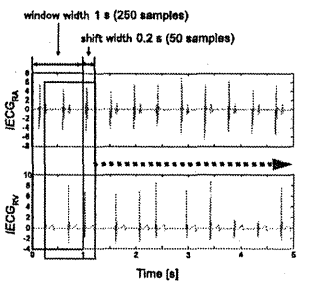

Fig. 2. Data acquisition using a 1 s long window shifting every 0.2 s

最初に，取得した心内心電図データに対して，0.8 Hz～40 Hzの帯域通過型フィルタを用いてノイズ成分を除去した。フィルタ処理後，Fig.2に示すように，1 sの長さの窓を用いて0.2 sずつシフトさせながらデータを抽出した。本研究では，窓ごとに心内心電図の特徴量に基づく指標を算出した。ここで，それぞれの心調律における窓の個数をTable 1に示す。Table 1からわかるように，SRが約67%を占め，その他の心調律の割合が低い。それゆえ，重回帰モデルの推定方法を工夫しないとSRの検出に特化したモデルとなってしまう可能性がある。

(倫理面への配慮)
実験に用いた成犬は，国立循環器病研究センター研究所の倫理委員会の規定に従って適切に管理され，実験は苦痛を与えない麻酔下で行われた。

* 東北大学大学院工学研究科
〒980-8578　宮城県仙台市青葉区荒巻字青葉6-3
Graduate School of Engineering, Tohoku University
6-3, Aoba, Aoba-ku, Sendai, Miyagi 980-8578, Japan
** 東北大学サイバーサイエンスセンター
〒980-8578　宮城県仙台市青葉区荒巻字青葉6-3
Cyberscience Center, Tohoku University
6-3, Aoba, Aoba-ku, Sendai, Miyagi 980-8578, Japan
*** 東北大学大学院医工学研究科
〒980-8578　宮城県仙台市青葉区荒巻字青葉6-3
Graduate School of Biomedical Engineering, Tohoku University
6-3, Aoba, Aoba-ku, Sendai, Miyagi 980-8578, Japan
**** オリンパス（株）
〒192-8512　東京都八王子市久保山町2-3
Olympus Corporation
2-3, Kuboyama-cho, Hachioji, Tokyo 192-8512, Japan
*5 国立循環器病研究センター研究所
〒565-8565　大阪府吹田市藤白台5-7-1
National Cerebral and Cardiovascular Center Research Institute
5-7-1, Fujishirodai, Suita, Osaka 565-8565, Japan
*6 九州大学大学院医学研究院
〒812-8582　福岡県福岡市東区馬出3-1-1
Graduate School of Medicine, Kyushu University
3-1-1, Maidashi, Higashi-ku, Fukuoka, Fukuoka 812-8582, Japan

Table 1. Number of windows and total duration of the data of each rhythm

	Number of windows	Duration [s]	Rate [%]
SR	3509	726.2	67.3
SVT	284	61.6	5.4
VT	474	102	9.1
VF	946	197.2	18.1

Table 2. Patterns of component ratio of each rhythm

	Pattern 1	Pattern 2	Pattern 3	Pattern 4
SR	random	25%	40%	55%
SVT	random	25%	20%	15%
VT	random	25%	20%	15%
VF	random	25%	20%	15%

〈2・2〉 不整脈の分類方法 本研究では，4種類の心調律の状態（SR，SVT，VT，VF）の判別を行うために，次のような，心内心電図の特徴量より得られる複数の指標を入力とした重回帰モデルに基づく方法を用いた[9][10]。

いま，上述のデータ窓における0.2 sの各シフトによって増加する離散時間をkとする。各データに対して，後述するm個の指標を求め，これらを要素とする$m \times 1$ベクトルを$\boldsymbol{x}(k)$とおく。また，4種類の心調律の種類SR，SVT，VT，およびVFに対応する番号をそれぞれ$i = 1, \ldots, 4$とするとき，心調律の分類を

$$y_i(k) = \begin{cases} 1 & \text{(if the sample belongs} \\ & \text{to the rhythm } i) \\ 0 & \text{(otherwise)} \end{cases} \quad \cdots\cdots (1)$$

で表す。$y_i(k)$を要素とする4×1ベクトル$\boldsymbol{y}(k) = [y_1(k), \ldots, y_4(k)]^{\mathrm{T}}$を検出ベクトルと呼ぶこととする。データベクトル$\boldsymbol{x}(k)$を説明変数とし，検出ベクトル$\boldsymbol{y}(k)$を目的変数とする重回帰モデルを

$$\boldsymbol{y}(k) = \boldsymbol{A}\boldsymbol{x}(k) + \boldsymbol{e}(k) \cdots\cdots (2)$$

で表す。ここで，$\boldsymbol{A}$は$4 \times m$行列であり，4×1ベクトル$\boldsymbol{e}(k)$は残差である。

本研究では，先行研究において実験的に有効性が確認された条件として，指標の数を$m = 14$，データ窓の個数を$K = 400$と定め，最小二乗法により(2)式の重回帰モデルの係数行列$\boldsymbol{A}$を計算した。

運用時には，逐次的に計算した各指標から作られる$\boldsymbol{x}(k)$を，(2)式で$\boldsymbol{e}(k) = 0$としたモデルに入力し，SR，SVT，VT，およびVFに対応する4つの目的変数$\boldsymbol{y}(k)$の推定値として検出結果ベクトル$\hat{\boldsymbol{y}}(k)$を計算する。それらの中の最大値に対応する心調律の番号iを，その時の心調律の種類として判定する。

先行研究では，全部でW個のデータ窓から無作為にK個のトレーニングデータを選択していたため，データ数の少ない心調律がトレーニングデータとして選ばれる確率は低かった。特にSVTは他の心調律に比べてデータ数が少なく，先行研究ではSVTの感度が低いモデルが推定されていた。そこで，本研究では，各心調律のトレーニングデータの割合をTable 2のような4種類のパターンを設定し，重回帰モデルの推定を行った。なお，Pattern 1は，先行研究で用いられている方法である。W個のデータをテストデータとし，推定された重回帰モデルの妥当性を検証するために用いた。

〈2・3〉 心内心電図に基づく指標 本研究では，重回帰モデルの入力として，先行研究[9][10]と同様，以下に示す14個の特徴量を用いた。

（1） Histogram: 心房と心室における心電図信号間の2次元ヒストグラムから求められる，Pearsonのχ^2統計量および標準偏差σ

（2） Period: $IECG_{\mathrm{LV}}$，$IECG_{\mathrm{RV}}$および$IECG_{\mathrm{RA}}$から得られる心周期とそれぞれの心周期間の比

（3） Delay: 2つの心電図間のR波検出における相対的な遅れ時間

（4） Complex: 2つの心電図をそれぞれ実部と虚部とする複素数と見なしたときの偏角と絶対値から求められる指標

〈2・4〉 過去の時系列を考慮した不整脈検出 本研究では，ある判定対象であるk番目の窓に対して，$\hat{\boldsymbol{y}}(k)$の最大値$\hat{y}_{\max}$が，あるしきい値$\hat{y}_{th}$より小さい場合，(3)式のように，その窓から過去n個の窓における検出結果ベクトルの値$\hat{\boldsymbol{y}}(k)$の平均を算出して判定を行う自己回帰フィルタを用いた。

$$\hat{\boldsymbol{y}}(k) \leftarrow \frac{\hat{\boldsymbol{y}}(k) + \hat{\boldsymbol{y}}(k-1) + \cdots \hat{\boldsymbol{y}}(k-n+1)}{n} \cdots\cdots (3)$$

この方法により，$\hat{y}_{\max}$が小さく信頼性が低い分類結果に対して，過去の判定結果の影響を及ぼすことで，誤判定を減らすことができると推察される。

本研究では，各パターンにおいて，致死性不整脈の不検出が最小，すなわち後述の偽陰性率が最小となるようなnを選択した。また，しきい値$\hat{y}_{th}$は，VFの不検出が起こる範囲に基づき，$\hat{y}_{th} = 0.7$と設定した。

加えて，VFの不検出を減らすために，複数窓の判定結果から1つの判定結果を確定する方法を導入する。先行研究[9][10]では窓のシフト幅である0.2 sごとに判定結果を出力していたが，本研究ではt_{det} [s]ごとに判定結果を出力する方法を検討する。提案方法では，複数個の窓における判定結果に対し，多数決関数を用いることで，1つの判定結果を$t_{\mathrm{det}} = 0.2, 0.4, \ldots, 3.0$ [s]ごとに出力することとした。この方法により，例えばVFの判定の中に突発的に出現したSRなどの誤判定を取り除くことができると考えられる。

〈2・5〉 検出性能の評価方法 提案アルゴリズムの有効性を評価するために，$W = 5213$個のデータ窓から，Table 2の4種類のパターンに基づいて，$K = 400$個の窓で区切られたトレーニングデータを選択し，重回帰モデルを推定した。さらに，提案方法のロバスト性を評価するため，先行研究[9][10]と同様にこの操作を100回繰り返し行い，偏回帰係数の平均値を算出することで平均モデルを求めた。そして，平均モデルを用いて全データ（$W = 5213$個）を対象とした心調律の分類を行った後，自己回帰フィルタを用いた分類および複数個の窓に対し多数決関数を用いた分類を段階的に適用した。

本研究では，自己回帰フィルタ適用後の判定結果と複数個の窓に対し多数決関数を用いたときの判定結果を個々に算出し，それぞれの提案方法に対する有効性の検証を行った。

それぞれのアルゴリズムの分類性能の評価を行うため，分類結果におけるそれぞれの心調律の感度と特異度を算出した。また，ICDが作動する場合（VT，VF）とそうでない場合（SR，SVT）に分けることで，偽陽性率および偽陰性率を算出し評価を行った。ここで，偽陽性率は誤分類によってICDが誤作動を起こす確率であり，SRとSVTのうちVTもしくはVFと誤って判定した窓数をSRとSVTの総窓数で割ることで算出される。一方，偽陰性率は誤分類によって致死性不整脈を見落とす確率であり，VTとVFのうちSRもしくはSVTと誤って判定した窓数をVTとVFの総窓数で割ることで算出される。

3. 結　果

まず，重回帰モデル推定後に自己回帰フィルタを適用して得られた分類結果のうち，各パターンにおける特異度をFig.3，感度をFig.4，偽陽性率ならびに偽陰性率をFig.5に示す。

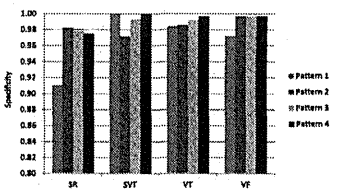

Fig. 3. Specificity of classification calculated from 4 pattern models

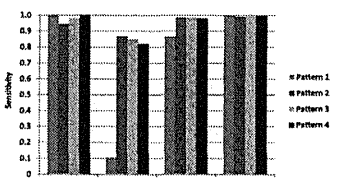

Fig. 4. Sensitivity of classification calculated from 4 pattern models

次に，自己回帰フィルタを適用した後に多数決関数を用いた複数個の窓の判定を行った場合の分類結果について，t_{det}を変化させたときの偽陽性率の変化をFig.6，偽陰性率の変化をFig.7に示す。

4. 考　察

Fig.3より，Pattern 1に比べてPattern 2〜4の方がSR，VT，VFの特異度が高いことがわかる。一方，SVTについてはPattern 2〜4の方が低い値であるが，これは，Pattern 1のときは，SVTが正しくモデル化できておらず，SVTと

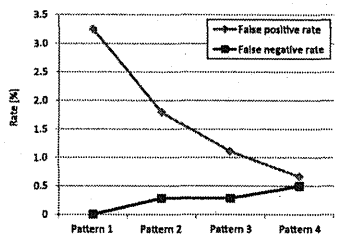

Fig. 5. False positive rate and false negative rate of classification calculated from 4 pattern models

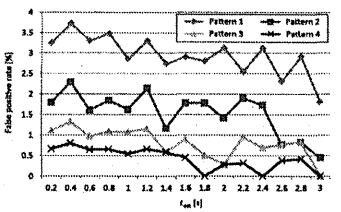

Fig. 6. False positive rate of classification using multiple windows

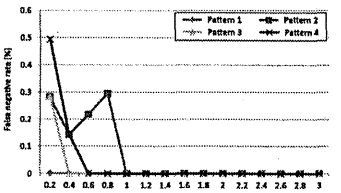

Fig. 7. False negative rate of classification calculated from 4 pattern models

判定される窓の数が少ないためである。

同様に，Fig.4 より，SR の比率を大きくすることで，SVT，VT の感度が上昇することがわかる。特に，SVT の感度の大幅な上昇がみられ，SR の比率を変更するというモデルの作成方法における有効性が確認された。

上述の結果から推察できるように，偽陽性率に関しては，Fig.5 より，Pattern 1 に比べて Pattern 2〜4 では低下する結果となり，SR や SVT の誤判定が減少している。一方で，偽陰性率に関しては，SR の比率の上昇とともに高くなる傾向があり，VF の不検出といった重大な誤判定が増加する可能性がある。

以上から，従来法に加えて，自己回帰フィルタを用いた解析方法では，Pattern 2〜4 において，SR や SVT の誤判定による ICD の誤作動が大幅に少なくなるものの，VF の不検出を伴う可能性があり，ICD への実装を考慮すると不十分な判定法であると考えられる。

次に，その問題点を解決する方法として用いた，多数決関数による複数個の窓の判定結果に基づく分類方法の結果について考察する。

Fig.6 より，t_{det} が大きくなるにつれて，偽陽性率は低下する傾向となった。また，SR の比率が大きいほど偽陽性率は低くなり，特に Pattern 4 では，$t_{det} = 1.8$ [s] のとき 0 となる。一方，Pattern 1〜3 では偽陽性率が 0 となるには 3 s 以上必要となるか，または 0 にならないため，Pattern 4 によるモデル作成方法の優位性が確認できる。

一方，偽陰性率については，Fig.7 より，$t_{det} = 1.0$ [s] のときすべての Pattern で 0 となり，提案手法によって VF 不検出の問題点が解消されていると考えられる。

これらの結果より，多数決関数を用いた複数個の窓による分類方法は，分類が確定するまで 1 s 程度の時間を要するものの，偽陰性率を 0 にし，偽陽性率を減少させることができる有用な方法であることが示された。特に Pattern 4 では $t_{det} = 1.8$ [s]，すなわち 9 個の窓の判定結果による多数決のときに偽陽性率，偽陰性率ともに 0 となり，有効性の高い手法であると推察される。さらに，既存の ICD の検出時間が 2〜3 s 程度[11][12]であることと比較して，致死性不整脈を早期に検出することが可能であるといえる。

これらの結果は，モデル作成に用いられるトレーニングデータにおける，心調律の比率による影響も大きいと考えられる。従来法で用いられた Pattern 1 のような無作為にテストデータを抽出する方法では，全データに含まれる心調律の比によってテストデータにおける心調律の比が決まる。そのため，全データに含まれる SVT や VT のような心調律の割合が小さい場合には，それらの心調律の特徴を十分に表すモデルを作成することが難しい。一方，本研究の提案方法では，4 つの心調律を特定の割合でテストデータとすることで，それぞれの心調律を特徴づける有効性の高いモデルを作成できたと推察される。

ただし，提案方法には次のような問題点もある。本方法では，重回帰モデルによる出力が正しい判定結果を示している場合においても，多数決関数の処理を行ってしまうため，冗長性が生じる可能性がある。そのため，VF 不検出に対する性能と処理の冗長性の関係について今後検討する必要がある。

5. おわりに

本研究では，不整脈の割合が SR に比べて小さいデータ群において，誤検出の少ない重回帰モデルの作成方法を提案した。また，VF の不検出や ICD の誤作動となる誤分類を減らすために過去の時系列を考慮した方法を提案した。提案した重回帰モデルの作成方法では，特に SVT や VT のようなデータ数の少ない心調律の検出精度の向上が認められた。さらに，自己回帰フィルタと多数決関数を適用することで，VF の不検出率を 0 に近づけることができ，偽陽性率を低下させることが可能となった。

提案したアルゴリズムについて，大幅な検出性能の向上が認められるが，論理的な複雑性から計算量の増加が問題となる可能性がある。そのため，ICD への実装を行う際には，計算量を抑える工夫を行って有効性を検証する必要がある。その検証の際には，重回帰モデルにおいて説明変数である指標の個数はどのくらいが最適であるか検証する必要がある。加えて，本研究で取り扱った 4 種類の心調律以外のデータに対しても，アルゴリズムがどのように動作するか検証をする必要性があると考えられる。

文　献

(1) 笠貫　宏：植込み型除細動器 (ICD) の歴史。日本心臓ペーシング・電気生理学会，植込み型除細動器調査委員会編，植込み型除細動器の臨床。医学書院，東京，p.1 (1998)

(2) 杉本恒明：突然死と不整脈，杉本恒明編，不整脈学，南江堂，東京，pp.12–14 (1992)

(3) A. Bayes de Luna, P. Coumel, and J.F. Leclercq: "Ambulatory sudden cardiac death: mechanisms of production of fatal arrhythmia on the basis of data from 157 cases", *Am. Heart J.*, Vol.117, No.1, pp.151–159 (1989)

(4) M. Mirowski, M.M. Mower, and P.R. Reid: "The automatic implantable defibrillator", *Am. Heart J.*, Vol.100, No.6, pt.2, pp.1089–1092 (1980)

(5) 大西　哲・笠貫　宏：ICD の原理と構造。田中栄夫編，心臓ペースメーカー・植込み型除細動器，メジカルビュー社，東京，pp.164–171 (2001)

(6) E. Aliot, R. Nitzsche, and A. Ripart: "Arrhythmia detection by dual-chamber implantable cardioverter defibrillators. A review of current algorithms", *Europace*, Vol.6, pp.273–286 (2004)

(7) K. Nanthakumar, M. Paquette, D. Newman, D.C. Deno, L. Malden, B. Gunderson, J. Gilkerson, M. Greene, D. Heng, and P. Dorian: "Inappropriate therapy from atrial fibrillation and sinus tachycardia in automated implantable cardioverter defibrillators", *Am. Heart J.*, Vol.139, pp.797–803 (2000)

(8) C. W. Israel: "How to avoid inappropriate therapy", *Current Opinion in Cardiology*, Vol.23, No.1, pp.65–71 (2008)

(9) 阿部　誠・テルマ　ケイコ　スガイ・吉澤　誠・山家智之・清水一夫・後藤　萌・稲垣正司・杉町　勝・砂川賢二：「重回帰分析を用いた致死性不整脈検出アルゴリズムに関する検討」，生体医工学，Vol.48, No.6, pp.577–583 (2010)

(10) 阿部　誠・テルマ　ケイコ　スガイ・吉澤　誠・本間経康・杉田典大・清水一夫・後藤　萌・稲垣正司・杉町　勝・砂川賢二：「植込み型除細動器用致死性不整脈検出アルゴリズムの高速・高精度化」，生体医工学，Vol.49, No.6, pp.932–938 (2011)

(11) M. Nair, N. Saoudi, D. Kroiss, and B. Letac: "Automatic arrhythmia identification using analysis of the atrioventricular association", *Circulation*, Vol.18, No.95, pp.967–973 (1997)

(12) E. G. Daoud, K. Nademanee, C. Fuenzalida, G.F. Tomassoni, C. Schuger, M. Chisner, M. Simones, M. Schwartz, and H. Reeve: "Clinical experience with tiered atrial therapies and atrial arrhythmia prevention algorithms in a dual chamber cardioverter defibrillator", *Journal of Cardiovascular Electrophysiology*, Vol.17, pp.852–856 (2006)

阿　部　　誠（正員）　2009 年東北大学大学院工学研究科博士後期課程修了。同年同大学サイバーサイエンスセンター厚生科研費研究員，11 年同大学工学研究科助教，現在に至る。映像の生体影響評価，致死性不整脈検出アルゴリズムの開発に関する研究に従事。博士（工学）。

吉　澤　　誠（非会員）　1983 年東北大学大学院工学研究科博士後期課程修了。同大学工学部助手，助教授，倉橋技術科学大学助教授，東北大学大学院助教授，同大学情報シナジーセンター教授を経て，現在，同大学サイバーサイエンスセンター教授。モバイル健診装置の開発に関する研究等に従事。工学博士。

テルマ　ケイコ　スガイ（非会員）　2011 年東北大学大学院医工学研究科博士後期課程修了。致死性不整脈検出アルゴリズムの開発，補助人工心臓装着時における心機能推定に関する研究に従事。博士（医工学）。

本　間　経　康（非会員）　1995 年東北大学大学院工学研究科博士後期課程修了。2000 年 Saskatchewan 大学客員教授などを経て，2003 年東北大学医学部助教授，2008 年同大学サイバーサイエンスセンター准教授，現在に至る。最適制御，腹雑系，脳科学，医用画像等の研究に従事。博士（工学）。

杉　田　典　大（非会員）　2004 年東北大学大学院工学研究科博士後期課程修了。2005 年，21 世紀 COE フェロー，2006 年，同大学工学研究科助手，助教を経て，現在，同大学工学研究科准教授。映像等の生体影響評価に関する研究等に従事。博士（工学）。

清　水　一　夫（非会員）　1983 年長岡技術科学大学大学院電気電子システム専攻科修了。1988 年オリンパス (株) 中途入社第 2 開発部所属，1998 年同社新事業推進本部 DM-pj グループリーダー（課長），同社研究開発企画部課長を経て，現在，同社医療技術開発本部医療探索部部長。医療機器の研究開発に従事。

後　藤　　萌（非会員）　2009 年東京大学大学院工学研究科修士課程修了。同年，オリンパス (株) 入社。現在，オリンパス株式会社医療技術開発本部医療探索部研究員。専門分野は生体信号処理。

稲　垣　正　司（非会員）　1987 年千葉大学医学部卒業。同年同大学医学部付属病院勤務，1991 年国立循環器病センター内科心臓部門，1996 年同研究所循環動態機能部研究員を経て，現在，国立循環器病研究センター研究所循環動態制御部室長。専門分野は循環器病学，不整脈学。

杉　町　　勝（非会員）　1984 年九州大学医学部卒業，1992 年論文博士取得。同年，国立循環器病センター研究所室長，2004 年同研究所部長を経て，現在，国立循環器病研究センター研究所循環動態制御部部長。心臓力学，循環動態，循環制御の研究，医療機器開発等に従事。博士（医学）。

砂　川　賢　二（非会員）　1974 年九州大学医学部卒業，論文博士取得。同大学医学部循環器内科医員，ジョンズホプキンス大学医学部研究生，講師，助教授，九州大学医学部助手，講師，国立循環器病センター研究所循環動態機能部長を経て，現在，九州大学大学院医学研究院循環器内科教授。専門分野はバイオニック心臓病学，心血管の力学等。医学博士。

INTERNATIONAL JOURNAL FOR NUMERICAL METHODS IN BIOMEDICAL ENGINEERING
Int. J. Numer. Meth. Biomed. Engng. (2012)
Published online in Wiley Online Library (wileyonlinelibrary.com). DOI: 10.1002/cnm.2522

Reproduction of pressure field in ultrasonic-measurement-integrated simulation of blood flow

Kenichi Funamoto*,† and Toshiyuki Hayase

Institute of Fluid Science, Tohoku University, 2-1-1 Katahira, Aoba-ku, Sendai 980-8577, Japan

SUMMARY

Ultrasonic-measurement-integrated (UMI) simulation of blood flow is used to analyze the velocity and pressure fields by applying feedback signals of artificial body forces based on differences of Doppler velocities between ultrasonic measurement and numerical simulation. Previous studies have revealed that UMI simulation accurately reproduces the velocity field of a target blood flow, but that the reproducibility of the pressure field is not necessarily satisfactory. In the present study, the reproduction of the pressure field by UMI simulation was investigated. The effect of feedback on the pressure field was first examined by theoretical analysis, and a pressure compensation method was devised. When the divergence of the feedback force vector was not zero, it influenced the pressure field in the UMI simulation while improving the computational accuracy of the velocity field. Hence, the correct pressure was estimated by adding pressure compensation to remove the deteriorating effect of the feedback. A numerical experiment was conducted dealing with the reproduction of a synthetic three-dimensional steady flow in a thoracic aneurysm to validate results of the theoretical analysis and the proposed pressure compensation method. The ability of the UMI simulation to reproduce the pressure field deteriorated with a large feedback gain. However, by properly compensating the effects of the feedback signals on the pressure, the error in the pressure field was reduced, exhibiting improvement of the computational accuracy. It is thus concluded that the UMI simulation with pressure compensation allows for the reproduction of both velocity and pressure fields of blood flow.

Received 10 April 2012; Revised 27 July 2012; Accepted 21 September 2012

KEY WORDS: bio-fluid mechanics; computational fluid dynamics; ultrasonic measurement; color Doppler imaging; measurement-integrated simulation

1. INTRODUCTION

Circulatory diseases such as heart disease and cerebrovascular disease are major causes of death. *In vivo* and *in vitro* experiments and numerical simulations of blood flow have been extensively carried out, indicating the relationships between diseases and hemodynamics [1, 2]. Blood flow information acquired by medical imaging techniques, such as ultrasonic measurement, magnetic resonance imaging (MRI) and computed tomography (CT), or directly measured by a catheter, sphygmomanometer or electrocardiogram is limited. On the other hand, blood flow simulation provides detailed information on three-dimensional unsteady hemodynamics including wall shear stress and pressure distributions. However, as it is inherently difficult to correctly specify the boundary and initial conditions, the computational results may differ from the real blood flow field data [3, 4]. Several methods have been proposed for flow simulation using defective boundary conditions, in which only flow rates are known [5, 6]. However, their efficiency for blood flow in a complicated vessel configuration remains to be investigated. Other factors, such as assumption of a rigid vessel wall, and uncertainties in vessel geometry, physical properties, and the model of the blood rheology, can also introduce errors into the computation. Consequently, at present, the diagnosis of circulatory diseases depends on empirical knowledge with limited measurement data. An innovative technique for accurate and detailed reproduction of blood flow field in a blood vessel is needed to realize more accurate and reliable diagnoses.

Various methodologies have been developed to computationally reproduce a flow field by integrating measurement and computation to overcome individual disadvantages. These methods include a method using proper orthogonal decomposition [7, 8], data assimilation based on Tichonov regularization [9], least-squares finite element methods [10, 11], the Kalman filter [12], variational methods [13, 14], and measurement-integrated (MI) simulation [15–18]. Data assimilation based on four-dimensional variation is widely used, especially in numerical weather forecasting [14]. However, it requires huge computational resources to repeatedly solve flow dynamics and its adjoint, and therefore, is not suitable for application to problems of real-time flow reproduction. In contrast, the Kalman filter and MI simulation are rather simple methods sequentially comparing the computational result with the corresponding measurement data and directly feeding back the differences to the numerical simulation. Compared with the Kalman filter, which usually employs a low-dimensional linear model, the MI simulation, which uses computational fluid dynamics as a mathematical model, can provide a solution with high accuracy once a convergent result is obtained although there is no systematic design method of the feedback signal. The authors have applied MI simulation to blood flow analysis by integrating medical measurement (ultrasonic measurement or phase-contrast MRI) and numerical simulation [19, 20]. With ultrasonic-measurement-integrated (UMI) simulation, the blood flow field is analyzed by applying artificial body forces proportional to the differences between the measured and computed Doppler velocities of the blood flow. Figure 1 shows a block diagram of the UMI simulation. Note that a 'Pressure compensation' block is newly added in this paper as explained in the following section. In our previous studies, a two-dimensional UMI simulation using real ultrasound color Doppler images was conducted [19]. The transient and steady characteristics of UMI simulation and the efficiency of feedback to reproduce unsteady three-dimensional hemodynamics were investigated by numerical experiments [21–23]. Those studies revealed that the UMI simulation improved computational accuracy in comparison with the ordinary simulation, making the computational velocity vector field approach that of a model solution of real blood flow. However, the reproducibility of the pressure field was not necessarily satisfactory [21, 24].

In this study, reproduction of the pressure field by UMI simulation was investigated. In the second section of this paper, the effect of feedback based on Doppler velocity on the pressure field is first examined by theoretical analysis, and a pressure compensation method is derived. In the third section, results of the theoretical analysis and the proposed pressure compensation method are validated by a numerical experiment dealing with a synthetic three-dimensional steady flow in a thoracic aneurysm.

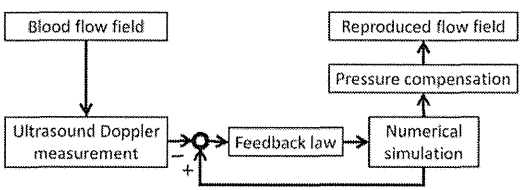

Figure 1. Block diagram of the UMI simulation.

*Correspondence to: Kenichi Funamoto, Institute of Fluid Science, Tohoku University, 2-1-1 Katahira, Aoba-ku, Sendai 980-8577, Japan.
†E-mail: funamoto@reynolds.ifs.tohoku.ac.jp

2. THEORETICAL ANALYSIS

The effect of the feedback signal on the pressure field in the UMI simulation is clarified by theoretical analysis, and a pressure compensation method is developed.

2.1. *Effect of feedback signals on the pressure field*

The governing equations of the UMI simulation of blood flow in a blood vessel are the Navier–Stokes equations and the equation of continuity.

$$\rho\left(\frac{\partial \mathbf{u}}{\partial t} + (\mathbf{u}\cdot\nabla)\,\mathbf{u}\right) = \mu\Delta\mathbf{u} - \nabla p + \mathbf{f}, \tag{1}$$

$$\nabla\cdot\mathbf{u} = 0, \tag{2}$$

where $\mathbf{u} = (u,\ v,\ w)$ is the velocity vector, p is the pressure, ρ is the density, μ is the viscosity, t is the time, and $\mathbf{f} = (f_x,\ f_y,\ f_z)$ is the external force term corresponding to the feedback signal. By substituting Equation (2) into the divergence of Equation (1), the pressure equation is derived as follows:

$$\Delta p = -\nabla\cdot\rho(\mathbf{u}\cdot\nabla)\,\mathbf{u} + \nabla\cdot\mathbf{f}. \tag{3}$$

Equations (1) and (3) are employed as the governing equations in the following analysis.

Regarding the boundary conditions, correct velocity profiles are assumed to be unknown, and a uniform or parabolic parallel profile with a known flow volume and free flow condition are specified at the upstream and downstream boundaries, respectively. The initial flow condition is an arbitrary flow field.

The feedback signal, $\mathbf{f}$, in Equation (1) is an artificial body force, which is proportional to the difference between the computed and measured Doppler velocities in the feedback domain defined in the computational domain:

$$\mathbf{f} = -K_v^*\frac{\Phi_d(\mathbf{u}-\mathbf{u}_s)}{U}\left(\frac{\rho U^2}{L}\right), \tag{4}$$

where K_v^* is the feedback gain (nondimensional), U is the characteristic velocity, L is the characteristic length, and $\mathbf{u}_s$ is the velocity vector of the real blood flow. Φ_d $(d = 1, 2, 3)$ is a projection function of a three-dimensional vector to the d-dimensional subspace [21]. The projection of the three-dimensional velocity vector in the direction of the ultrasonic beam in the UMI simulation corresponds to the case of $d = 1$, and $\Phi_1(\mathbf{u})$ and $\Phi_1(\mathbf{u}_s)$ correspond to computed and measured Doppler velocities, respectively. Here, measurement errors, such as noise, contained in ultrasonic Doppler measurement are ignored for simplicity. Note that, in our previous study [23], the effects of major measurement errors on the computational accuracy of the UMI simulation were investigated, and methods to compensate those effects were proposed. The special case with $K_v^* = 0$ corresponds to the ordinary numerical simulation without feedback.

Previous studies [21–23] have revealed that with a proper application of feedback, the computational velocity field approaches the real velocity field of the blood flow. Generally, because a velocity field has a unique pressure field, it was expected that the computational pressure field would concurrently approach the real pressure field. However, the reproducibility of pressure field was not necessarily satisfactory.

The pressure field by the UMI simulation is discussed in the following. The velocity field, $\mathbf{u}_s$, and the pressure field, p_s, of a real blood flow satisfy governing Equations (1) and (3) without the external force term, $\mathbf{f}$, with the upstream and downstream boundary conditions of the correct velocity profiles and with the initial condition of the correct velocity vector field at the first time step:

$$\rho\left(\frac{\partial \mathbf{u}_s}{\partial t} + (\mathbf{u}_s\cdot\nabla)\,\mathbf{u}_s\right) = \mu\Delta\mathbf{u}_s - \nabla p_s, \tag{5}$$

$$\Delta p_s = -\nabla\cdot\rho(\mathbf{u}_s\cdot\nabla)\,\mathbf{u}_s. \tag{6}$$

DOI: 10.1002/cnm

In the UMI simulation, incorrect specification of boundary conditions introduces error to the computational result as compared with the real blood flow, but the feedback based on Doppler velocity works to reduce the error in the velocity vector field in the feedback domain. Therefore, in the equation derived from the subtraction of Equation (6) from Equation (3), the velocity vector, $\mathbf{u}$, is approximately equal to the real velocity vector, $\mathbf{u}_s$, and the following equation is approximately satisfied in the feedback domain:

$$\Delta p = \Delta p_s + \nabla\cdot\mathbf{f}. \tag{7}$$

This equation implies that the pressure field, p, of the UMI simulation becomes different from the real pressure field, p_s, because of the effect of feedback in the case that the divergence of the feedback force vector is not zero.

2.2. *Pressure compensation method*

A pressure compensation method for the UMI simulation is introduced. The pressure compensation is applied after the convergent results of velocity and pressure are obtained (see Figure 1). The correct pressure field, p_s, is expressed as the summation of the computational result, p, and the compensation term, p_f.

$$p_s = p + p_f. \tag{8}$$

With Equation (7) and Equation (8) operated by Laplacian operator, the following equation is obtained.

$$\Delta p_f = -\nabla\cdot\mathbf{f}. \tag{9}$$

The pressure compensation, p_f, is calculated from Equation (9) by setting zero value at the boundaries of the computation domain. In the case that the blood flow is considered to be parallel flow such as the one in a straight blood vessel, pressure is constant over the cross-section perpendicular to the flow. In addition, if the flow rate in the UMI simulation is identical to that of the real flow, the pressure differences between upstream and downstream boundaries are the same between the cases. Consequently, the boundary conditions of the pressure equations for p and p_s can be considered to be the same. Because $p_f = p_s - p$ from Equation (8), the value of p_f should be zero at the upstream and downstream boundaries. By substituting the pressure compensation, p_f, into Equation (8), an estimated value, p_s', of the correct pressure is obtained.

The proposed pressure compensation method is equivalent to a modification of the UMI simulation retaining only the divergence-free part of the feedback signal, $\mathbf{f}_{div}$. The feedback signal, $\mathbf{f}$, can be decomposed to an irrotational part, $\mathbf{f}_{irr}$, and a divergence-free part, based on Helmholtz decomposition [25]. Pressure compensation, p_f, obtained from Equation (9) determines the irrotational part of the feedback signal as $\mathbf{f}_{irr} = -\nabla p_f$, which does not contribute to improvement of the computational accuracy of the velocity field, but deteriorates that of the pressure field.

2.3. *Discretization*

Outlines of discretization of the governing equations of the UMI simulation, including the pressure compensation equation, are described in this section. The above-mentioned governing equations are discretized by means of the finite volume method and are solved with the SIMPLER method [26]. The concrete notations of the parameters in the following equations, and supplementary pressure correction equations and velocity correction procedure in the SIMPLER method, are explained in [26].

The x-directional momentum equation in Navier–Stokes equations of Equation (1):

$$B_p u_{i,j,k} = \sum B_{nb}u_{nb} + S_{i,j,k} + A_i(p_{i-1,j,k} - p_{i,j,k}) + \Delta V_{i,j,k} f_{x_{i,j,k}}, \tag{10}$$

where Bs are the elements of the matrix consisting of all of the diffusive terms and a part of the convective terms in the discretized Navier–Stokes equation, and $(\sum B_{nb}u_{nb})$ is the summation of

DOI: 10.1002/cnm

the values at six adjacent nodes in the three-dimensional computation. The second term, $S_{i,j,k}$, on the right side is the source term, which consists of a part of the convective terms and a part of the time-derivative term. The third term is the pressure gradient term in which A_i is the cross-sectional area of the control volume, and the last term is the feedback term in which $\Delta V_{i,j,k}$ is the volume of the cell. Subscript p denotes the position where $u(i,\ j,\ k)$ is defined, and nb means adjacent nodes. Equations for y-directional and z-directional momentums are analogous to that in Equation (10).

The pressure equation of Equation (3):

$$C_P p_{i,j,k} = \sum C_{nb} p_{nb} + S_{pi,j,k} + S_{fi,j,k}, \tag{11}$$

where Cs are the elements of the matrix derived from discretization of the pressure equation, $S_{pi,j,k}$ is the source term derived from discretization of the first term on the right side of Equation (3), and $S_{fi,j,k}$ is the source term because of the feedback. Subscript P denotes the position where $p(i,\ j,\ k)$ is defined. The source term because of the feedback, $S_{fi,j,k}$, is denoted in the following equation:

$$S_{fi,j,k} = \frac{\rho}{B_p}[(f_{x\,i,j,k} - f_{x\,i+1,j,k})A_i + (f_{y\,i,j,k} - f_{y\,i,j+1,k})A_j + (f_{z\,i,j,k} - f_{z\,i,j,k+1})A_k], \tag{12}$$

where A_i, A_j, and A_k are the cross-sectional areas of the control volume facing each direction.

Pressure compensation for feedback of Equation (9):

Equation (9) is also expressed in a way similar to the pressure equation

$$C_p p_{fi,j,k} = \sum C_{nb} p_{fnb} - S_{fi,j,k}, \tag{13}$$

where coefficients C_p and C_{nb}, and the source term $S_{fi,j,k}$ are identical with those in Equations (11) and (12).

3. VALIDATION WITH NUMERICAL EXPERIMENT

Results of the theoretical analysis and the proposed pressure compensation method are validated by a numerical experiment dealing with a synthetic three-dimensional steady flow in a thoracic aneurysm. Ultrasonic measurement provides the Doppler velocity necessary for the feedback in UMI simulation, but it does not provide other information necessary for evaluating the UMI simulation such as three-dimensional velocity vectors or pressure field. Hence, we do not use real measurement data for the reference data. Instead, we use a numerical solution for a synthetic steady flow with realistic upstream and downstream velocity boundary conditions called 'standard solution' as a model of real blood flow to perform the numerical experiment. The boundary conditions of the standard solution are determined from a preliminary simulation of blood flow in a whole aorta including an aneurysm. Reproduction of the standard solution by the UMI simulations with/without the pressure compensation and the ordinary numerical simulation without feedback are investigated. The numerical simulations conducted in this section are summarized in Table I.

Table I. Classification of preliminary simulation (PS), standard solution (SS), UMI simulation (UMIS), and ordinary simulation (OS).

Name	Solver	Domain	Grid	Boundary velocity	Feedback	Note
PS	FLUENT	Whole aorta Figure 2(a)	Hexahedral 142,417	Uniform inlet Free stream outlet	N/A	Boundary velocity for SS was obtained.
SS	Original (SIMPLER)	Aneurysm Figure 2(b)	Orthogonal $40 \times 34 \times 49$	Specified velocity inlet & outlet	N/A	Model of real flow
UMIS	Original (SIMPLER)	Aneurysm Figure 2(b)	Orthogonal $40 \times 34 \times 49$	Uniform inlet Free stream outlet	Applied	Measurement data was was generated by SS.
OS	Original (SIMPLER)	Aneurysm Figure 2(b)	Orthogonal $40 \times 34 \times 49$	Uniform inlet Free stream outlet	N/A	

DOI: 10.1002/cnm

3.1. Methods

A numerical experiment was conducted to investigate the computational accuracy of the pressure field by the UMI simulation and to examine the efficiency of the proposed pressure compensation method. The objective was a steady flow in a thoracic aneurysm, which was the same as in a previous study [22]. A steady numerical solution with realistic boundary conditions was first defined as the standard solution. The boundary conditions of the standard solution were determined from a preliminary simulation of blood flow in a whole aorta including the aneurysm. Although generation of synthetic measurement data for validation of new algorithms has been investigated [27,28], the computational three-dimensional velocity vectors were simply projected in the direction of the ultrasonic beam without consideration of measurement errors to obtain the Doppler velocity of the standard solution. Then, with inaccurate boundary conditions but with the correct flow volume, UMI simulation and an ordinary simulation without feedback were performed. In the UMI simulation, Doppler velocities of the standard solution were used for feedback. After the convergent results of velocity and pressure were obtained, the pressure compensation was applied to the pressure field (see Figure 1).

A preliminary simulation for a whole aorta was first performed. The configuration of the whole aorta from the ascending aorta to the abdominal aorta, including an aneurysm in the descending aorta, was reconstructed, as shown in Figure 2(a), by accumulating X-ray CT images (Aquilion 16, Toshiba, Tokyo, Japan) of a 76-year-old female patient with commercial three-dimensional reconstruction software (Mimics 7.3, Materialise, Leuven, Belgium) [22]. A preliminary simulation of a steady blood flow in the whole aorta (Figure 2(a)) was carried out by using commercial computational fluid dynamics software (FLUENT 6.1.22, Fluent, Inc., Lebanon, NH). The computational grid used in the preliminary FLUENT simulation consisted of 142,417 hexahedral elements. Pressure–velocity coupling was accomplished by the SIMPLE method, and spatial discretization schemes were employed as follows: a Green-Gauss cell-based scheme for gradient; a standard scheme for pressure; and a first-order upwind for momentum. Uniform velocity was applied at the inlet boundary so that the average flow rate became 8.65×10^{-5} m^3/s, and a

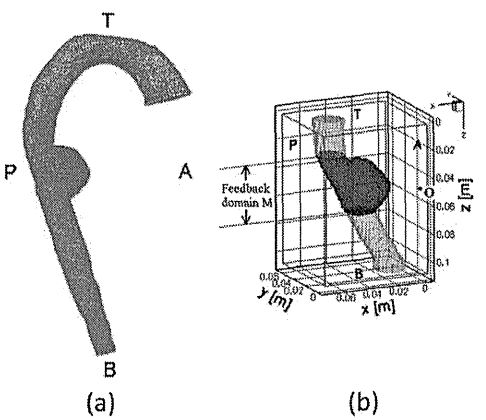

Figure 2. Computational grids for (a) a preliminary simulation of a steady flow in the whole aorta with an aneurysm in the descending aorta by using FLUENT, and for (b) the other simulations of the flow in the partial domain including the aneurysm with a feedback domain (dark gray zone) and a probe position at O.

DOI: 10.1002/cnm

free-flow condition was applied at the downstream boundary. A no-slip condition was set on the wall. The convergence criterion in the numerical simulation was set at 1×10^{-4} for momentum and continuity equations.

In the following computations for the standard solution, the UMI simulation, and the ordinary simulation, the computational domain was limited to the vicinity of the thoracic aneurysm, as shown in Figure 2(b). A computational grid system was generated by introducing a staggered grid system of $40 \times 34 \times 49$ grid points in x, y, and z directions, compromising reproducibility of vessel configuration and computational load. The grid interval dz in the z direction was set at 2.00×10^{-3} m, which was the same as the slice interval of the X-ray CT, and those in the other directions were determined to be $dx = dy = 1.78 \times 10^{-3}$ m. The equivalent diameter of the blood vessel, D, at the upstream boundary calculated by averaging x-directional and y-directional maximum lengths of the cross-section of the blood vessel at the upstream boundary was 23.47×10^{-3} m. Flow rate was set at 8.65×10^{-5} m^3/s (same as the preliminary simulation), and the average flow velocity at the upstream boundary, U, was 2.00×10^{-1} m/s. The density, ρ, and viscosity, μ, of the blood were assumed to be 1.00×10^3 kg/m^{3}and 4.00×10^{-3} Pa$\cdot$s, respectively. All the variables were nondimensionalized with the equivalent diameter of the blood vessel, D, as the characteristic length, L, the average flow velocity as the characteristic velocity, U, and the density of blood, ρ, as the characteristic density. The Reynolds number of the steady flow was 1174. From here on, the same symbols are used for both dimensional and nondimensional values because it does not cause any confusion.

In the computation of the standard solution, velocity profiles at the upstream and downstream boundaries were determined as those on the corresponding cross-sections of the preliminary simulation. In the UMI simulation and the ordinary simulation, a uniform parallel flow was applied at the upstream boundary, and the free flow condition was set at the downstream boundary.

Because the computational result converges to the target flow with the aid of the feedback process, unsteady flow computation is required for the UMI simulation even for the present steady target flow. Time-dependent computation was performed for all cases. The computational time increment was set as $\Delta t = 0.01(1.17 \times 10^{-3}$ s) [22].

In UMI simulation, considering the acquisition of Doppler velocities in the three-dimensional domain by transesophageal ultrasonography, the ultrasound probe or the origin of ultrasonic beam was set at O[$(x, y, z) = (0.008, 0.023, 2.045)$((0.000 m, 0.001 m, 0.048 m))], which was located at the same height as the aneurysm, as shown in Figure 2(b). The Doppler beam direction was along a line from the origin of ultrasonic beam to each computational gird point. Blood flow in the whole aneurysmal domain M[$1.193 \leqslant z \leqslant 2.897$(0.028 m $\leqslant z \leqslant$ 0.068 m), shown by a dark gray zone in Figure 2(b)], including the parent blood vessel, was assumed to be measured. Domain M was defined as the feedback domain, and at all the grid points in the fluid region of domain M, feedback signals were added to the UMI simulation based on the differences of Doppler velocities between the simulation and the standard solution.

In the computation of the standard solution, the UMI simulation and the ordinary simulation, the governing equations were discretized by the finite volume method and were solved with an original program based on the SIMPLER method [26, 29] as described in the previous section. The convective terms were discretized with the reformulated QUICK scheme [30], and the time derivative terms were discretized with the first Euler implicit scheme. Linear algebraic equations were solved using the modified strongly implicit (MSI) scheme [31]. The convergence criterion in the numerical simulation was set at 1×10^{-4} for momentum and continuity equations.

To evaluate the computational accuracy of the UMI simulation and the ordinary simulation, a space-averaged error norm of a variable, a (velocity vector, $\mathbf{u}$, or pressure, p), in a monitoring domain Ω was defined by the following equation:

$$\bar{e}_\Omega(a,t) = \frac{1}{N} \sum_{X_n \in \Omega} \left| \frac{a_{cn}(t) - a_{sn}(t)}{a_{\mathrm{ref}}} \right|, \tag{14}$$

where n and N are the identification number and the total number of the monitoring points, respectively, $|\cdot|$ is the absolute value for scalar variables or the l_1 norm, $|u| + |v| + |w|$, for velocity vector $\mathbf{u}$, and a_{ref} is the characteristic value for normalization: $a_{\mathrm{ref}} = U$ for velocity or $a_{\mathrm{ref}} = \rho U^2$

DOI: 10.1002/cnm

for pressure. Subscripts, c and s, means UMI simulation or ordinary simulation and the standard solution, respectively.

3.2. Results and discussion

The results of the UMI simulation with/without pressure compensation were evaluated by error norms of the velocity vector and pressure in feedback domain M (or the aneurysmal domain), $\bar{e}_{\mathrm{M}}(\mathbf{u}, t)$ and $\bar{e}_{\mathrm{M}}(p, t)$, and compared with those of the ordinary numerical simulation. The variations of $\bar{e}_{\mathrm{M}}(\mathbf{u}, t)$ and $\bar{e}_{\mathrm{M}}(p, t)$ of the UMI simulations at $K_{\mathrm{v}}^* = 0$, 80 and 160 are shown in Figure 3. The UMI simulations diverge at $K_{\mathrm{v}}^* \geqslant 170$ in the case of $\Delta t = 0.01$ as revealed in our previous study [22]. There is an inversely proportional relationship between the time increment and the maximum feedback gain. Concerning this issue, we theoretically clarified that the feedback signal in the source term destabilized the iterative calculation, and proposed a computational scheme to remove the destabilization phenomenon [32]. However, we used the previous scheme in this study because improvement of computational accuracy of pressure can be discussed in a stable region with the feedback gain of $K_{\mathrm{v}}^* < 170$. In the case of $K_{\mathrm{v}}^* = 0$, which corresponds to the ordinary simulation without feedback, neither error norm temporally changes because the steady solution was set as the initial condition (a dotted line in Figure 3). In contrast, by applying feedback in the UMI simulations at $K_{\mathrm{v}}^* = 80$ and 160, the error norm of the velocity vector, $\bar{e}_{\mathrm{M}}(\mathbf{u}, t)$, monotonically decreases and converges at each constant value (dashed and solid black lines in Figure 3(a)). This indicates that the velocity field of the UMI simulation is closer to the standard solution than that of the ordinary

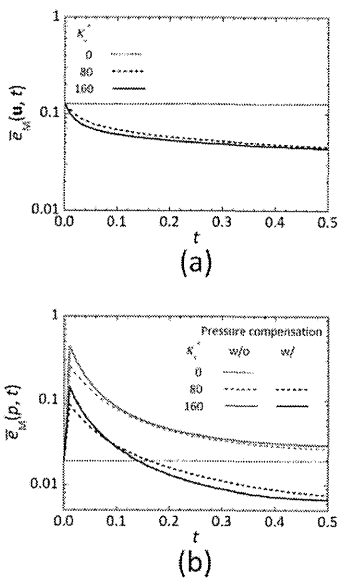

Figure 3. Transient changes of space-averaged error norms of (a) velocity vector and (b) pressure in the feedback domain in the UMI simulations without/with pressure compensation at $K_{\mathrm{v}}^* = 0$, 80, and 160 (nondimensional).

DOI: 10.1002/cnm

simulation. Moreover, the larger feedback gain reduces the error more rapidly. On the other hand, the error norm of pressure, $\bar{e}_M(p,\ t)$, of the UMI simulations without pressure compensation drastically increases at the first time step ($t = 0.01$), and then decreases toward each constant value (dashed and solid gray lines in Figure 3(b)). With either feedback gain, the convergent value of $\bar{e}_M(p,\ t)$ remains larger than that of the ordinary simulation, indicating deterioration of the computational accuracy of the pressure field by the feedback. Generally, improvement of the computational accuracy of the velocity field leads to better reproduction of the pressure field as time progresses. However, as described in the theoretical analysis, pressure error against the standard solution arises because the feedback signals do not become zero so as to reduce the error derived from a constant difference of the boundary conditions. The results of $\bar{e}_M(p,\ t)$ by the UMI simulations at $K_v^* = 80$ and 160 with pressure compensation are presented with dashed and solid black lines in Figure 3(b), respectively. In the time of $t > 0.2$, the error norms of the pressure of the UMI simulations are smaller than that of the ordinary simulation. This means that the pressure field approaches the standard solution, cancelling the error in the pressure field caused by feedback signals. Moreover, the UMI simulation with a large feedback gain $\left(K_v^* = 160\right)$ presents a larger value of $\bar{e}_M(p,\ t)$ than that of the UMI simulation with a small feedback gain $\left(K_v^* = 80\right)$ at the beginning of the computation, but it finally gives a smaller convergent value.

The variations of steady values of the space-averaged error norms of the velocity vector and pressure in the feedback domain M, $\bar{e}_M(\mathbf{u},\ t_\infty)$ and $\bar{e}_M(p,\ t_\infty)$ ($t_\infty = 20$), with the feedback gain are shown in Figure 4. In the UMI simulation, the value of $\bar{e}_M(\mathbf{u},\ t_\infty)$ monotonically decreases

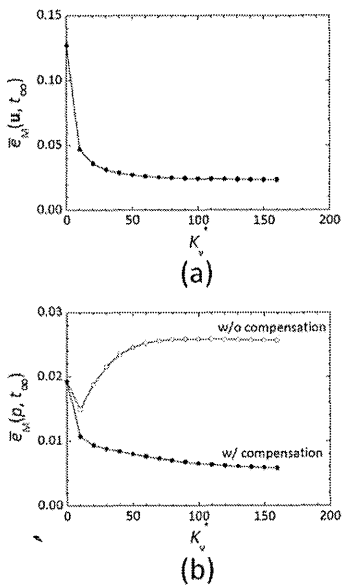

Figure 4. Variations of steady values of space-averaged error norms of (a) velocity vector and (b) pressure in the feedback domain with feedback gain (nondimensional).

DOI: 10.1002/cnm

with increasing feedback gain (Figure 4(a)). Note that the error norm of the velocity vector in the UMI simulation is not affected by the pressure compensation. However, the value of $\bar{e}_M(p,\ t_\infty)$ at first decreases and then increases (open circle plots in Figure 4(b)). In $K_v^* > 20$, the error norm is larger than that of the ordinary simulation $\left(K_v^* = 0\right)$. When the feedback gain is relatively small $\left(K_v^* < 20\right)$, the computational accuracy of the pressure field seems to be improved in accordance with the improvement of that of the velocity field because the pressure deviation as a result of the application of artificial body forces (or feedback signals) is not significant. With large feedback gain, however, the ability to reproduce the pressure field deteriorates because the significant artificial body forces proportional to the feedback gain are applied. In contrast, as the feedback gain increases, the value of $\bar{e}_M(p,\ t_\infty)$ after the pressure compensation monotonically decreases, similar to that of the velocity vectors (solid circle plots in Figure 4(b)). This reflects the fact that the pressure field concurrently becomes closer to the standard solution with the velocity field. Regarding the determination of the feedback gain, K_v^*, in the practical application of the UMI simulation, although the UMI simulation with a large feedback gain reduces the error against the measurement data, it reproduces the measurement error as well. In our previous study [23], the effects of major measurement errors on the computational accuracy of the UMI simulation were investigated, and methods to compensate those effects were proposed. An appropriate value of the feedback gain should be determined based on the results, considering how much compensation is achieved. It is also noted that the UMI simulation has sufficiently high frequency response characteristics to ensure the convergence to the unsteady flow [22].

The result of the UMI simulation at $K_v^* = 160$ is further investigated in the following. The steady values of the space-averaged error norms of velocity vector and pressure against the standard solution in each z-directional cross-section, $\bar{e}_{cs(z)}(\mathbf{u},\ t_\infty)$ and $\bar{e}_{cs(z)}(p,\ t_\infty)$ ($t_\infty = 20$), in the ordinary simulation $\left(K_v^* = 0\right)$ and the UMI simulations without/with the pressure compensation are shown in Figure 5(a) and (b), respectively. The dotted line and the gray and black solid lines represent the results of the ordinary simulation and the UMI simulations without and with the pressure compensation, respectively, and the gray area indicates the feedback domain in the UMI simulation. Compared with the ordinary simulation, in the case of the UMI simulations, the error norm of the velocity vector, $\bar{e}_{cs(z)}(\mathbf{u},\ t_\infty)$, is decreased after the feedback domain ($z \geq 1.193$), and remains smaller in a certain downstream region of the feedback domain ($2.897 < z < 3.8$), as shown by the solid lines in Figure 5(a). Regarding the error norm of pressure, $\bar{e}_{cs(z)}(p,\ t_\infty)$, shown in Figure 5(b), the UMI simulation with the pressure compensation presented a smaller value than the ordinary simulation in all z-directional cross-sections and almost the same value near the downstream boundary, implying the ability to reproduce the pressure field with good accuracy. On the other hand, the error norm of pressure, $\bar{e}_{cs(z)}(p,\ t_\infty)$, in the UMI simulation without pressure compensation increases in the upstream region of the feedback domain and exceeds that of the ordinary simulation with the peak value near the upstream boundary of the feedback domain. It then decreases in the downstream direction and becomes the same as that in the UMI simulation with the pressure compensation. Figure 5(c) shows a summation of absolute values of the divergence of the feedback force vector in each z-directional cross-section. The value is large in the upstream side in the feedback domain where the error in the velocity field is large, especially at the upstream boundary of the feedback domain where feedback signals discontinuously change. Moreover, in comparison with Figure 5(b), the large value of the divergence of the feedback force vector also influences the computational accuracy of the pressure field in the upstream domain before the feedback domain where the divergence is zero.

The pressure distributions on a y-directional cross-section ($y = 1.462$) of the standard solution, the ordinary simulation $\left(K_v^* = 0\right)$, and the UMI simulations $\left(K_v^* = 160\right)$ without/with the pressure compensation are depicted in Figure 6. Between the pressure fields of the standard solution and the ordinary simulation, p_s and p_o (Figures 6(a) and (b)), a difference can be observed near the upstream boundary, but similar pressure profiles are obtained in the aneurysm. As observed in the error norm of pressure in Figure 5(b), the UMI simulation without pressure compensation (Figure 6(c)) provides a pressure distribution different from that of the standard solution (Figure 6(a)), especially in the upstream region of the feedback domain (see an arrow), but it gives almost the same distribution in the aneurysm. In the UMI simulation with the pressure compensation (Figure 6(d)),

DOI: 10.1002/cnm

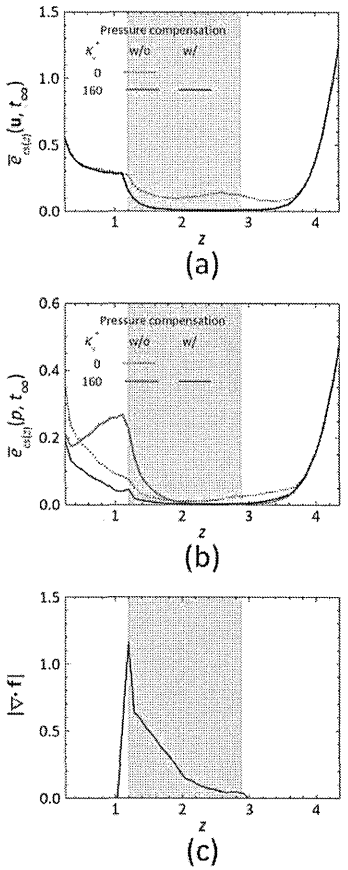

Figure 5. Steady values of space-averaged error norms of (a) velocity vector and (b) pressure, and (c) space-averaged absolute value of divergence of feedback signal vector in each z-directional cross-section (nondimensional). The gray zone implies the feedback domain.

the difference in pressure distribution observed in the UMI simulation without the pressure compensation is properly improved.

The distributions of error norm of pressure against the standard solution on the corresponding y-directional cross-section are shown in Figure 7. As mentioned above, the ordinary simulation and the UMI simulation without the pressure compensation show relatively large error near the upstream

DOI: 10.1002/cnm

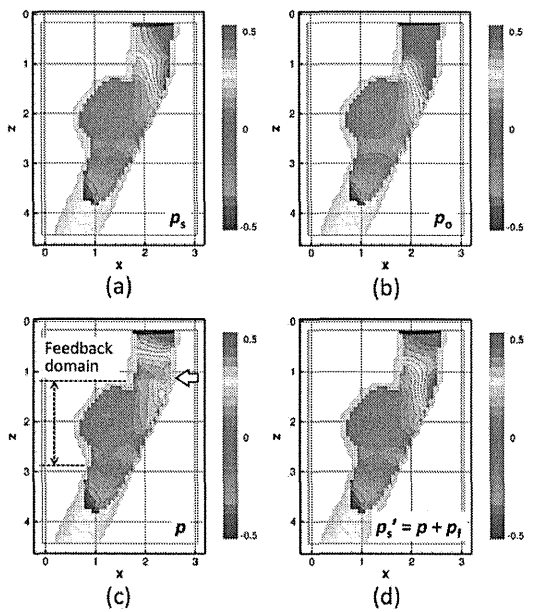

Figure 6. Pressure distribution on a y-directional cross-section ($y = 1.462$): (a) standard solution, p_s, (b) ordinary simulation ($K_v^* = 0$), p_o, and UMI simulations (c) without and (d) with pressure compensation at $K_v^* = 160$, p and p_s', respectively (nondimensional).

boundary and in the vicinity of the upstream boundary of the feedback domain, respectively. In contrast, the error in the UMI simulation with the pressure compensation is relatively small in the whole domain.

The distribution of the divergence of the feedback force vector in the UMI simulation is demonstrated in Figure 8(a). There is a region with a large magnitude of divergence of the feedback force vector near the upstream boundary of the feedback domain. Figure 8(b) shows the distribution of the pressure compensation in the UMI simulation, p_f, calculated from Equation (9). It is noted that the distribution of the pressure compensation has a pattern similar to that of the error norm of the pressure for the UMI simulation without the pressure compensation in Figure 7(b). By adding the pressure compensation, p_f (Figure 8(b)), to the result of the UMI simulation without compensation (Figure 6(c)), a compensated pressure field, p_s' (Figure 6(d)), is obtained.

In summary, the numerical experiment dealing with a three-dimensional steady flow in a thoracic aneurysm indicates that feedback signals in the UMI simulation can deteriorate the reproducibility of the pressure field, while improving that of the velocity field. However, by properly compensating the effects of the feedback signals on the pressure with the proposed method, both the velocity and pressure fields of the standard solution can be properly reproduced.

DOI: 10.1002/cnm

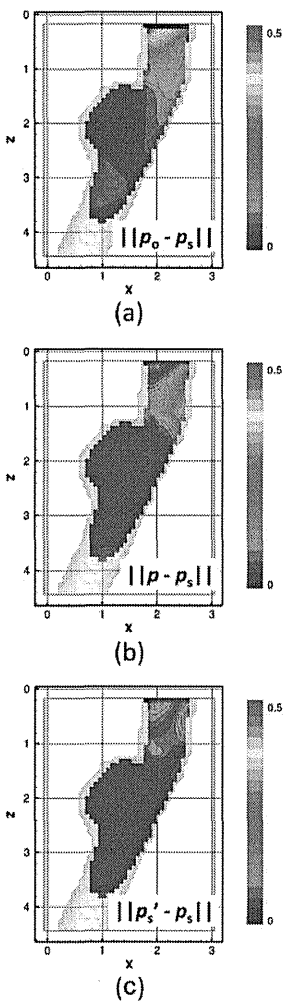

Figure 7. Error norm of pressure on a y-directional cross-section ($y = 1.462$): (a) ordinary numerical simulation $(K_v^* = 0)$, and UMI simulations (b) without and (c) with pressure compensation at $K_v^* = 160$, respectively (nondimensional).

DOI: 10.1002/cnm

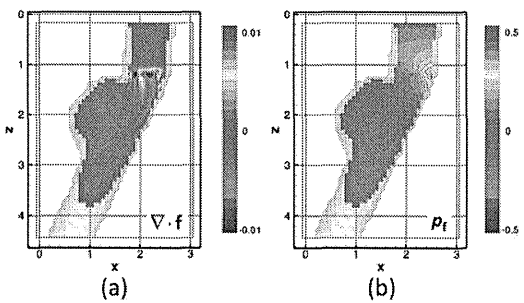

Figure 8. Distributions of (a) divergence of feedback force vector and (b) value for pressure compensation, p_f, in the UMI simulation at $K_v^* = 160$ (nondimensional).

4. CONCLUSION

In this study, reproduction of the pressure field by UMI simulation was investigated. The effect of feedback based on Doppler velocity on the pressure field was first examined by theoretical analysis. When the divergence of the feedback force vector was not zero, it influenced the pressure field in the UMI simulation, while improving the computational accuracy of the velocity field. Hence, a method to estimate the correct pressure by compensating the pressure field was devised. A numerical experiment was conducted dealing with the reproduction of a three-dimensional steady flow in a thoracic aneurysm to validate results of the theoretical analysis. The ability of the UMI simulation to reproduce the pressure field deteriorated with a large feedback gain. However, by properly compensating the effects of the feedback signals on the pressure, the error in the pressure field was reduced, exhibiting improvement of the computational accuracy in comparison with that of the ordinary simulation. Hence, the UMI simulation with pressure compensation allows for the reproduction of both velocity and pressure fields of blood flow. The information on hemodynamic stresses (wall shear stress and pressure) and blood flow dynamics enables a better understanding of blood flow and would provide novel indices for diagnosis of diseases. To perform the UMI simulation in a clinical setting, further investigations on automatic excursion of the sequential computation including reconstruction of the blood vessel configuration and recognitions of the position and orientation of the ultrasound probe are required.

REFERENCES

1. Friedman MH, Krams R, Chandran KB. Flow interactions with cells and tissues: cardiovascular flows and fluid-structure interactions. *Annals of Biomedical Engineering* 2010; **38**:1178–1187.
2. Taylor CA, Steinman DA. Image-based modeling of blood flow and vessel wall dynamics: applications, methods and future directions. *Annals of Biomedical Engineering* 2010; **38**:1188–1203.
3. Morris L, Delassus P, Grace P, Wallis F, Walsh M, McGloughlin T. Effects of flat, parabolic and realistic steady flow inlet profiles on idealised and realistic stent graft fits through Abdominal Aortic Aneurysms (AAA). *Medical Engineering & Physics* 2006; **28**:19–26.
4. Moyle KR, Antiga L, Steinman DA. Inlet conditions for image-based CFD models of the carotid bifurcation: is it reasonable to assume fully developed flow? *Journal of Biomechanical Engineering-Transactions of the ASME* 2006; **128**:371–379.
5. Formaggia L, Gerbeau JF, Nobile F, Quarteroni A. Numerical treatment of defective boundary conditions for the Navier-Stokes equations. *SIAM Journal on Numerical Analysis* 2002; **40**:376–401.
6. Veneziani A, Vergara C. An approximate method for solving incompressible Navier-Stokes problems with flow rate conditions. *Computer Methods in Applied Mechanics and Engineering* 2007; **196**:1685–1700.

DOI: 10.1002/cnm

7. McGregor RH, Szczerba D, von Siebenthal M, Muralidhar K, Szekely G. Exploring the use of proper orthogonal decomposition for enhancing blood flow images via computational fluid dynamics. *Medical Image Computing and Computer Assisted Intervention* 2008; **11**:782–789.
8. McGregor RH, Szczerbal D, Muralidhar K, Szekely G. A fast alternative to computational fluid dynamics for high quality imaging of blood flow. *Medical Image Computing and Computer Assisted Intervention* 2009; **12**:124–131.
9. Zeldin BA, Meade AJ. Integrating experimental data and mathematical models in simulation of physical systems. *AIAA Journal* 1997; **35**:1787–1790.
10. Dwight RP. Bayesian inference for data assimilation using least-squares finite element methods. *IOP Conference Series: Materials Science and Engineering* 2010; **10**:012224.
11. Heys JJ, Manteuffel TA, McCormick SF, Milano M, Westerdale J, Belohlavek M. Weighted least-squares finite elements based on particle imaging velocimetry data. *Journal of Computational Physics* 2010; **229**:107–118.
12. Bertoglio C, Moireau P, Gerbeau JF. Sequential parameter estimation for fluid-structure problems. Application to hemodynamics. *International Journal for Numerical Methods in Biomedical Engineering* 2012; **28**:434–455.
13. D'Elia M, Perego M, Veneziani A. A variational data assimilation procedure for the incompressible Navier-Stokes equations in hemodynamics. *Journal of Scientific Computing* 2012; **52**:340–359.
14. Munro R, Kopken C, Kelly G, Thepaut JN, Saunders R. Assimilation of Meteosat radiance data within the 4D-Var system at ECMWF: data quality monitoring, bias correction and single-cycle experiments. *Quarterly Journal of the Royal Meteorological Society* 2004; **130**:2293–2313.
15. Hayase T, Hayashi S. State estimator of flow as an integrated computational method with the feedback of online experimental measurement. *Journal of Fluids Engineering-Transactions of the ASME* 1997; **119**:814–822.
16. Nisugi K, Hayase T, Shirai A. Fundamental study of hybrid wind tunnel integrating numerical simulation and experiment in analysis of flow field. *JSME International Journal Series B-Fluids and Thermal Engineering* 2004; **47**:593–604.
17. Yamagata T, Hayase T, Higuchi H. Effect of feedback data rate in PIV measurement-integrated simulation. *Journal of Fluid Science and Technology* 2008; **3**:477–487.
18. Nakao M, Kawashima K, Kagawa T. Application of MI simulation using a turbulent model for unsteady orifice flow. *Journal of Fluids Engineering-Transactions of the ASME* 2009; **131**:111401.
19. Funamoto K, Hayase T, Shirai A, Saijo Y, Yambe T. Fundamental study of ultrasonic-measurement-integrated simulation of real blood flow in the aorta. *Annals of Biomedical Engineering* 2005; **33**:415–428.
20. Funamoto K, Suzuki Y, Hayase T, Kosugi T, Isoda H. Numerical validation of MR-measurement-integrated simulation of blood flow in a cerebral aneurysm. *Annals of Biomedical Engineering* 2009; **37**:1105–1116.
21. Funamoto K, Hayase T, Saijo Y, Yambe T. Numerical experiment for ultrasonic-measurement-integrated simulation of three-dimensional unsteady blood flow. *Annals of Biomedical Engineering* 2008; **36**:1383–1397.
22. Funamoto K, Hayase T, Saijo Y, Yambe T. Numerical experiment of transient and steady characteristics of ultrasonic-measurement-integrated simulation in three-dimensional blood flow analysis. *Annals of Biomedical Engineering* 2009; **37**:34–49.
23. Funamoto K, Hayase T, Saijo Y, Yambe T. Numerical analysis of effects of measurement errors on ultrasonic-measurement-integrated simulation. *IEEE Transactions on Biomedical Engineering* 2011; **58**:653–663.
24. Funamoto K, Hayase T, Saijo Y, Yambe T. Numerical study on variation of feedback methods in ultrasonic-measurement-integrated simulation of blood flow in the aneurysmal aorta. *JSME International Journal Series C-Mechanical Systems, Machine Elements and Manufacturing* 2006; **49**:144–155.
25. Arfken GB, Weber HJ. *Mathematical Methods for Physicists*. Elsevier Academic Press: Amsterdam/Boston/Tokyo, 2005.
26. Patankar SV. *Numerical Heat Transfer and Fluid Flow*. Hemisphere Pub. Corp.: Washington DC/New York, 1980.
27. Morbiducci U, Ponzini R, Rizzo G, Biancolini ME, Iannaccone F, Gallo D, Redaelli A. Synthetic dataset generation for the analysis and the evaluation of image-based hemodynamics of the human aorta. *Medical & Biological Engineering & Computing* 2012; **50**:145–154.
28. Swillens A, De Schryver T, Lovstakken L, Torp H, Segers P. Assessment of numerical simulation strategies for ultrasonic color blood flow imaging, based on a computer and experimental model of the carotid artery. *Annals of Biomedical Engineering* 2009; **37**:2188–2199.
29. Hayase T, Humphrey JAC, Greif R. Mini-manual for ROTFLO2. *Department of Mechanical Engineering Report*, University of California, Berkeley, 1990; FM-90-1.
30. Hayase T, Humphrey JAC, Greif R. A consistently formulated QUICK scheme for fast and stable convergence using finite-volume iterative calculation procedures. *Journal of Computational Physics* 1992; **98**:108–118.
31. Schneider GE, Zedan M. A modified strongly implicit procedure for the numerical solution of field problems. *Numerical Heat Transfer* 1981; **4**:1–19.
32. Hayase T, Imagawa K, Funamoto K, Shirai A. Stabilization of measurement-integrated simulation by elucidation of destabilizing mechanism. *Journal of Fluid Science and Technology* 2010; **5**:632–647.

DOI: 10.1002/cnm

Eur J Nucl Med Mol Imaging (2013) 40:125–132
DOI 10.1007/s00259-012-2261-2

ORIGINAL ARTICLE

Comparison of the binding characteristics of [^{18}F]THK-523 and other amyloid imaging tracers to Alzheimer's disease pathology

Ryuichi Harada · Nobuyuki Okamura · Shozo Furumoto · Tetsuro Tago · Masahiro Maruyama · Makoto Higuchi · Takeo Yoshikawa · Hiroyuki Arai · Ren Iwata · Yukitsuka Kudo · Kazuhiko Yanai

Received: 1 May 2012 / Accepted: 21 September 2012 / Published online: 26 October 2012

Abstract
Purpose Extensive deposition of senile plaques and neurofibrillary tangles in the brain is a pathological hallmark of Alzheimer's disease (AD). Although several PET imaging agents have been developed for in vivo detection of senile plaques, no PET probe is currently available for selective detection of neurofibrillary tangles in the living human brain. Recently, [^{18}F]THK-523 was developed as a potential in vivo imaging probe for tau pathology. The purpose of this study was to compare the binding properties of [^{18}F]THK-523 and other amyloid imaging agents, including PiB, BF-227 and FDDNP, to synthetic protein fibrils and human brain tissue.
Methods In vitro radioligand binding assays were conducted using synthetic amyloid β_{42} and K18ΔK280-tau fibrils. Nonspecific binding was determined by the addition of unlabelled compounds at a concentration of 2 μM. To examine radioligand binding to neuropathological lesions, in vitro autoradiography was conducted using sections of AD brain.
Results [^{18}F]THK-523 showed higher affinity for tau fibrils than for Aβ fibrils, whereas the other probes showed a higher affinity for Aβ fibrils. The autoradiographic analysis indicated that [^{18}F]THK-523 accumulated in the regions containing a high density of tau protein deposits. Conversely, PiB and BF-227 accumulated in the regions containing a high density of Aβ plaques.
Conclusion These findings suggest that the unique binding profile of [^{18}F]THK-523 can be used to identify tau deposits in AD brain.

Keywords PET probes · Tau · Amyloid · Alzheimer's disease

Electronic supplementary material The online version of this article (doi:10.1007/s00259-012-2261-2) contains supplementary material, which is available to authorized users.

R. Harada · N. Okamura (✉) · S. Furumoto · T. Yoshikawa · K. Yanai
Department of Pharmacology, Tohoku University School of Medicine, 2-1, Seiryo-machi, Aoba-ku, Sendai 980-8575, Japan
e-mail: nookamura@med.tohoku.ac.jp

S. Furumoto · T. Tago · R. Iwata
Division of Radiopharmaceutical Chemistry, Cyclotron and Radioisotope Center, Tohoku University, Sendai, Japan

M. Maruyama · M. Higuchi
Molecular Imaging Center, National Institute of Radiological Sciences, Chiba, Japan

H. Arai
Department of Geriatrics and Gerontology, Institute of Development, Aging and Cancer, Tohoku University, Sendai, Japan

Y. Kudo
Innovation of New Biomedical Engineering Center, Tohoku University, Sendai, Japan

Introduction

Senile plaques and neurofibrillary tangles (NFTs) composed of amyloid-β (Aβ) peptides and aggregated tau proteins, respectively, are the pathological hallmarks of Alzheimer's disease (AD). In vivo amyloid imaging techniques have received a lot of attention for their promise in presymptomatic detection of Aβ pathology [1]. Recently, several β-sheet binding radiotracers have been developed as PET amyloid imaging agents [2]. Among them, ^{18}F-labelled 2-(1-{6-[(2-fluoroethyl(methyl)amino)-2-naphthyl)ethylidene)malononitrile ([^{18}F]FDDNP) was the first PET probe to be applied to clinical PET imaging in patients with AD [3]. This tracer demonstrated higher regional uptake in the medial temporal lobe and neocortex, and was claimed to bind to Aβ and tau pathological lesions [3]. Subsequently, ^{11}C-labelled 2-[4′-(methylamino)phenyl]-6-hydroxybenzothiazole ([^{11}C]PiB) and 2-(2-[dimethylaminothiazole-5-yl]ethenyl)-6-(2-[fluoro]ethoxy)benzoxazole ([^{11}C]BF-227) were also developed as amyloid imaging radiotracers. These tracers bind to Aβ fibrils with high affinity [4] and have demonstrated a significantly higher retention in the neocortical areas of brains of AD patients than of healthy controls [5, 6]. Furthermore, post-mortem analysis of AD patients who had undergone [^{11}C]PiB PET imaging before death suggested a strong correlation between in vivo PiB binding and regional distribution of Aβ plaques [7].

Amyloid imaging with PET can detect AD pathology in its preclinical stage [8]. However, amyloid deposition as assessed by [^{11}C]PiB PET correlates poorly with cognitive impairment in AD [9, 10], whereas deposition of tau in the medial temporal cortex is closely associated with neuronal death in this region. Selective tau imaging would provide important information about the tau pathophysiological features in AD, allowing correlation of brain tau load with cognitive decline, monitoring of disease progression and evaluation of therapeutic efficacy of newly developed therapies. Potential candidates for in vivo tau imaging agents include quinoline derivatives [11], and in a recent study, we found that one quinoline derivative, [^{18}F]THK-523, showed higher affinity for tau rather than amyloid fibrils. Furthermore, an autoradiography analysis indicated that this tracer binds specifically to tau deposits but not Aβ burden at tracer concentrations usually achieved during a PET scan [12].

The binding profiles of PiB, BF-227 and FDDNP to Aβ fibrils have been well described. Because tau, α-synuclein and prion fibrils, as well as Aβ fibrils, share a common β-sheet secondary structure, these compounds can potentially bind all these misfolded proteins. A previous study indicated that PiB binds to both Aβ and PHF tau pathology in vitro [13]. However, the binding occurs at higher concentrations than usually achieved in vivo during a PET scan. Furthermore, PET–pathology correlation studies have demonstrated that PiB binding reflects Aβ pathology [7, 14]. Newly developed ^{18}F-labelled amyloid PET tracers have similarly shown good correlation with Aβ plaque density [15, 16]. However, the binding affinity of these radiotracers for tau fibrils remains unknown and the binding properties of [^{18}F]THK-523 have not been directly compared with those of other amyloid PET agents. Here, we compared the binding affinity of [^{18}F]THK-523 to synthetic Aβ and tau protein fibrils as well as to senile plaques and NFTs in human brain samples with those of PiB, BF-227 and FDDNP, to characterize the binding properties of THK-523 and to obtain a better understanding of current and future PET data.

Materials and methods

Materials

The nonlabelled compounds PiB, BF-227, FDDNP, THK-523 (Fig. 1) and their precursors were custom-synthesized by Tanabe R&D Service (Osaka, Japan). Human $A\beta_{42}$ was purchased from Peptide Institute Inc. (Mino, Japan). Recombinant K18ΔK280-tau protein was obtained from Invitrogen (Tokyo, Japan).

Radiolabelling of PiB, BF-227, THK-523 and FDDNP

[^{3}H]PiB (specific activity 2.96 GBq/μmol) was purchased from American Radiolabeled Chemicals (St. Louis, MO). [^{11}C]PiB was radiolabelled using its precursor (2-(4-aminophenyl)-6-methoxymethoxybenzothiazole) and [^{11}C]methyl triflate, as

Fig. 1 Chemical structures of [^{11}C]PiB, [^{18}F]FDDNP, [^{11}C]BF-227 and [^{18}F]THK-523

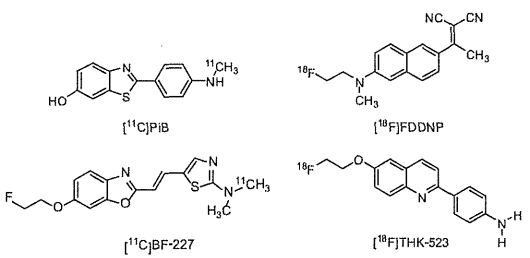

previously described [17, 18]. The mean specific activity of [^{11}C]PiB was 34.6 GBq/μmol.

[^{18}F]BF-227 was synthesized by nucleophilic substitution of the tosylate precursor (2-[2-(2-dimethylaminothiazol-5-yl)ethenyl]-6-[2-(tosyloxy)ethoxy]benzoxazole. After a 10-min reaction at 110 °C, the crude mixture was partially purified on an activated Sep-Pak tC18 cartridge before being purified by semi-preparative reverse-phase HPLC. Standard tC18 Sep-Pak reformulation produced [^{18}F]BF-227 in >95 % purity. The radiochemical yield was 12–19 % (non-decay-corrected), and the mean specific activity of [^{18}F]BF-227 was 163 GBq/μmol at the end of the synthesis. [^{11}C]BF-227 was synthesized using *N*-desmethylated derivatives as its precursor and [^{11}C]methyl triflate, as previously described [6]. The mean specific activity of [^{11}C]BF-227 was 136 GBq/μmol.

[^{18}F]THK-523 was synthesized by nucleophilic substitution of the tosylate precursor (2-(4-aminophenyl)-6-(2-tosyloxyethoxy)quinolone) as previously described [12]. The standard tC18 Sep-Pak reformulation produced [^{18}F]THK-523 in >95 % purity. The radiochemical yield was 38–49 % (non-decay-corrected), and the mean specific activity of [^{18}F]THK-523 was 68 GBq/μmol at the end of the synthesis.

[^{18}F]FDDNP was radiolabelled by the nucleophilic substitution of the tosylate precursor (2-{[6-(2,2-dicyano-1-methylvinyl)-2-naphthyl](methyl)amino}ethyl-4-methylbenzenesulphonate) as previously described [19]. After a 15-min reaction at 95 °C, the crude mixture was partially purified on an activated Sep-Pak tC18 cartridge before being purified by semipreparative reverse-phase HPLC. Standard tC18 Sep-Pak reformulation produced [^{18}F]FDDNP in >95 % purity. The radiochemical yield was 12–19 % (non-decay-corrected), and the mean specific activity of [^{18}F]FDDNP was 27 GBq/μmol at the end of the synthesis. All analysis HPLC chromatograms are shown in the Supplementary figure.

In vitro radioligand binding assays

Synthetic $A\beta_{42}$ fibrils and K18ΔK280-tau fibrils were prepared as previously described [12]. For in vitro binding assays, synthetic $A\beta_{42}$ or K18ΔK280 fibrils (200 nM) were incubated with increasing concentrations of [^{3}H]PiB and ^{18}F-labelled compounds (0.5–200 nM). To account for nonspecific binding of [^{3}H]PiB and ^{18}F-labelled compounds, the above-mentioned reactions were performed in triplicate in the presence of each unlabelled compound at a concentration of 2 μM.

The binding reactions were incubated for 1 h for the ^{18}F-labelled compounds and 3 h for [^{3}H]PiB at room temperature, in 200 μL of assay buffer (Dulbecco's PBS, 0.1 % BSA). Separation of bound from free radioactivity was achieved by filtration under reduced pressure (MultiScreen HTS Vacuum Manifold, MultiScreen HTS 96-well 0.65-μm filtration plate; Millipore, Billerica, MA). The filters were washed three times with 200-μL assay buffer, and the filters containing the bound ^{18}F-labelled compounds were then assayed for radioactivity in a γ counter (AccuFLEX γ7000, Aloka, Tokyo, Japan). The filters containing [^{3}H]PiB were incubated in 2 mL of scintillation fluid (Aquasol-2; PerkinElmer, Boston, MA), and the radioactivity of ^{3}H was counted using a β counter (LS6500 liquid scintillation counter; Beckman Coulter, Brea, CA). The binding data were analysed with curve-fitting software that calculated the K_D and B_{max} using nonlinear regression (GraphPad Prism version 5.0; GraphPad Software, San Diego, CA).

Autoradiography, immunohistochemistry and Gallyas silver staining

Demographics of post-mortem brain samples are shown in Table 1. The frontal and medial temporal brain sections (6 μm thick) of three AD patients were incubated with 1.0 MBq/mL ^{11}C-labelled and ^{18}F-labelled compounds at room temperature for 10 min and then washed briefly with water and 50 % ethanol. After drying, the labelled sections were exposed to a BAS-III imaging plate (Fuji Film, Tokyo, Japan) overnight. The autoradiographic images were obtained using a BAS-5000 phosphoimaging instrument (Fuji Film) with a spatial resolution of 25×25 μm. The adjacent sections were immunostained using AT8 anti-tau monoclonal antibody (diluted 1:20; Innogenetics, Ghent, Belgium) and 6F/3D (diluted 1:50; Dako, Glostrup, Denmark). The adjacent sections were also stained by the Gallyas-Braak method, which has been reported to be NFT-specific [20].

Results

Binding affinity for synthetic Aβ and tau fibrils

To characterize the binding properties of THK-523, PiB, BF-227 and FDDNP, in vitro radioligand binding assays for synthetic $A\beta_{42}$ and truncated tau construct (K18ΔK280) fibrils were performed under the same experimental conditions. Truncated tau construct (K18ΔK280) consists of the four repeat regions (244–372) but lacking lysine 280 (ΔK280) observed in FTLD-17 familial mutation.

Table 1 Demographics of brain samples used in this study

Brain no.	Age (years)	Sex	Post-mortem interval (h)
AD1	76	F	16
AD2	82	F	17
AD3	92	F	8.5

K18ΔK280 tau aggregates exhibit the similar characteristic as PHF-tau from AD brain [21]. In addition, K18ΔK280 tau forms aggregates quickly without cofactor such as heparin [22]. Thus, we used K18ΔK280 fibrils for the in vitro binding assays. Our analysis indicated that [^{18}F]THK-523 had a higher binding affinity for tau fibrils (K_{D1} = 1.99 ± 0.21 nM, B_{max1} = 1.22 ± 0.24 pmol THK-523/nmol K18ΔK280-tau) than for $A\beta_{42}$ fibrils (K_{D1} = 30.3 ± 3.91 nM, B_{max1} = 12.6 ± 0.45 pmol THK-523/nmol $A\beta_{42}$), which was similar to previously published data [12]. On the other hand, [^{3}H]PiB bound to $A\beta_{42}$ fibrils with high affinity (K_{D1} = 0.84 ± 0.18 nM, B_{max1} = 0.44 ± 0.07 pmol PiB/nmol $A\beta_{42}$). [^{3}H]PiB also showed two binding sites for K18ΔK280-tau fibrils, but with a lower affinity (K_{D1} = 6.39 ± 1.63 nM, B_{max1} = 1.38 ± 0.48 pmol PiB/nmol K18ΔK280) than [^{18}F]THK-523. [^{18}F]BF-227 showed a high binding affinity for $A\beta_{42}$ fibrils (K_{D1} = 1.72 ± 0.83 nM, B_{max1} = 0.50 ± 0.14 pmol BF-227/nmol $A\beta_{42}$), similar to our previous report [23], but showed a lower affinity for tau fibrils (K_D = 30.2 ± 2.29 nM, B_{max} = 10.7 ± 0.24 pmol BF-227/nmol K18ΔK280-tau). [^{18}F]BF-227 had an approximately 20-fold higher affinity for the first class of $A\beta_{42}$ binding sites compared with tau fibrils. Only one class of [^{18}F]FDDNP binding site was identified on the $A\beta_{42}$ (K_D = 5.52 ± 1.97 nM, B_{max} = 0.277 ± 0.06 pmol FDDNP/nmol $A\beta_{42}$) and K18ΔK280 tau fibrils (K_D = 36.7 ± 11.6 nM, B_{max} = 2.14 ± 0.46 pmol FDDNP/nmol K18ΔK280-tau). These results suggest that [^{18}F]FDDNP binds $A\beta_{42}$ fibrils with lower affinity than [^{3}H]PiB and [^{18}F]BF-227. Furthermore, [^{18}F]FDDNP had an approximately sevenfold higher affinity for $A\beta_{42}$ fibrils than for tau fibrils. These binding profiles are significantly different from that of [^{18}F]THK-523 (Table 2).

In vitro autoradiography of human brain sections

To further assess the binding selectivity of [^{18}F]THK-523, autoradiographic images of the frontal (Fig. 2) and medial temporal (Fig. 3) brain sections from three AD patients, using [^{18}F]THK-523, [^{11}C]PiB and [^{11}C]BF-227, were compared. While Aβ plaques in the frontal grey matter were labelled with [^{11}C]PiB (Fig. 2a–c) and [^{11}C]BF-227 (Fig. 2g–i), the binding of [^{18}F]THK-523 in the frontal grey matter (Fig. 2m–o) was considerably lower. In the medial temporal brain sections, [^{11}C]PiB (Fig. 3a–c) and [^{11}C]BF-227 (Fig. 3g–i) did not accumulate in the hippocampal CA1 area, whereas [^{18}F]THK-523 (Fig. 3m–o) did accumulate in this area (Fig. 3m–o). The presence of a high density of tau and a low density of Aβ in this area was confirmed by immunohistochemistry (Fig. 3d–f, j–l). Furthermore, the band-like distribution of [^{18}F]THK-523 in the inner layer of the temporal grey matter was similar to the distribution of tau (Fig. 3j–l). In the high-magnification images of case AD3 (Fig. 3p–v), the distribution of [^{18}F]THK-523 closely resembled Gallyas silver staining and tau immunostaining. [^{18}F]THK-523 binding was observed in the areas showing a high density of NFTs in the hippocampal CA1, the layer pre-α and pri-α in the entorhinal cortex (ERC) (Fig. 3p, q, r, t). Intriguingly, [^{18}F]THK-523 labelling in the layer pre-α of the ERC corresponded to Gallyas silver staining better than tau immunostaining, suggesting the preferential binding of [^{18}F]THK-523 to extracellular tau deposits that were clearly visualized by Gallyas silver staining [25]. In contrast to [^{18}F]THK-523, the distribution of [^{11}C]PiB was similar to that of Aβ immunohistochemistry (Fig 3q, u, v). [^{11}C]PiB binding corresponded to the formation of amyloid in the parvopyramidal layer of the presubicular area and in the layers pre-β and pre-γ of the ERC (Fig. 3s, v) [26].

Discussion

In the study reported here, we for the first time directly compared the binding properties of the novel quinoline derivative THK-523 and other amyloid PET probes. Our data suggest the potential utility of THK-523 for the selective detection of PHF-tau in the living human brain, which has not previously been achieved. The autoradiographic images of sections from AD brains revealed that [^{18}F]THK-523 successfully labelled PHF-tau deposits but did not label Aβ deposits in the frontal and temporal cortices. These findings suggest that [^{18}F]THK-523 is a promising

Table 2 K_D and B_{max} values of [^{3}H]PiB, [^{18}F]BF-227, [^{18}F]FDDNP and [^{18}F]THK-523 for K18ΔK280-tau and $A\beta_{42}$ fibrils

Compound	K18ΔK280 fibrils				$A\beta_{42}$ fibrils			
	K_{D1}	B_{max1}	K_{D2}	B_{max2}	K_{D1}	B_{max1}	K_{D2}	B_{max2}
[^{18}F]THK-523	1.99±0.21	1.22±0.24	50.7±2.73	4.55±0.74	30.3±3.91	12.6±0.45	–	–
[^{18}F]BF-227	30.2±2.29	10.7±0.24	–	–	1.72±0.83	0.50±0.14	56.1±25.1	13.4±4.37
[^{18}F]FDDNP	36.7±11.6	2.14±0.46	–	–	5.52±1.97	0.277±0.06	–	–
[^{3}H]PiB	6.39±1.63	1.38±0.48	304±77.4	20.6±11.2	0.84±0.18	0.44±0.07	60.6±8.32	26.1±8.57

K_D values are in nanomoles, and B_{max} values are in picomoles compound per nanomole fibrils (n=3).